Design and Implementation of Efficient Terahertz Waveguides

by

Hamid Pahlevaninezhad
B.Sc., Isfahan University of Technology, 2002
M.Sc., Amirkabir University of Technology, 2005

A Dissertation Submitted in Partial Fulfillment
of the Requirements for the Degree of

DOCTOR OF PHILOSOPHY

in the Department of Electrical and Computer Engineering

Supervisory Committee

Design and Implementation of Efficient Terahertz Waveguides

by

Hamid Pahlevaninezhad
B.Sc.., Isfahan University of Technology, 2002
M.Sc., Amirkabir University of Technology, 2005

Supervisory Committee

Dr. Thomas Edward Darcie, (Department of Electrical and Computer Engineering)
Supervisor

Dr. Jens Bornemann, (Department of Electrical and computer Engineering)
Departmental Member

Dr. Colin Bradley (Department of Mechanical Engineering)
Outside Member

Abstract

Supervisory Committee

Dr. Thomas Edward Darcie, (Department of Electrical and Computer Engineering)
Supervisor

Dr. Jens Bornemann, (Department of Electrical and Computer Engineering)
Departmental Member

Dr. Colin Bradley, (Department of Mechanical engineering)
Outside Member

In this thesis, novel broadband waveguides capable of operating at terahertz (THz) frequencies are introduced. We explore in detail the two-wire waveguide showing that it can have absorption as low as 0.01 cm^{-1}, fairly good coupling efficiency, and is free from group-velocity dispersion (GVD). We also propose two low loss, planar slot-line structures for guiding THz waves. Rigorous theoretical analyses, numerical simulations, and experimental results are presented to evaluate and verify the performance of the waveguides at THz frequencies. We also present a tapered structure to couple effectively THz waves from a photoconductive source to a two-wire waveguide. Finally, practical structures to realize the first THz low-loss cable using the two-wire waveguide are introduced.

Table of Contents

List of Figures

Acknowledgments

I would like to thank my special wife, Mehrnoush, for always being with me and supporting me. She has tolerated me when I had to study and had no time for her and I really appreciate that. Her encouraging and supporting attitude is priceless to me.

I would also like to give my special thanks to my supervisor, Dr. T. E. Darcie, for being supportive and helping me go through challenges in my studies. I have always enjoyed my discussions with him as his positive attitude makes them constructive. He always is looking for what we can do to make things work rather than what we could have done and we did not. I also want to thank my good friends in OSTL Lab at the University of Victoria, specially Barmak Heshmat and James Zhang. I want to thank Dr. R. Gordon for letting me use the facilities in his lab.

Chapter 1

Introduction

The terahertz wavelength range, between 30-1000 μm, is located between microwave and infrared frequencies, as shown in Fig. 1.1. This frequency range has been one of the least explored regions of the electromagnetic spectrum. This could be attributed to the lack of practical sources and detectors of terahertz radiation.

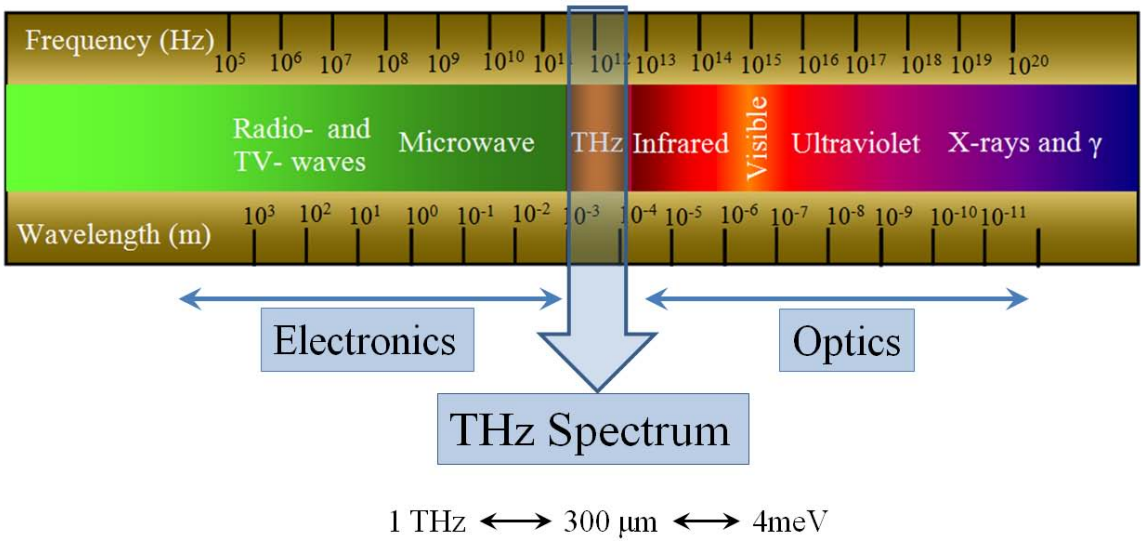

Figure 1.1 Terahertz spectrum.

1.1 THz Applications

The general interest in terahertz frequencies rose mainly due to unique abilities in spectroscopy and imaging, contributing to new tools for exploring material properties and several biomedical applications. Other techniques using visible and near-infrared radiation have been extensively employed in studying such effects. However, many basic excitations in strongly correlated electron systems occur at terahertz frequencies, motivating the use of terahertz spectroscopy [1,2]. There are numerous applications for THz waves in areas like security, inspection, and spectroscopy. These applications

benefit from short wavelength and unique penetration and absorption of photons in the THz wavelength range.

For biomedical applications, THz imaging can reveal the contrast between regions of healthy skin and Basal Cell Carcinoma (BCC) [3]. THz waves are capable of penetrating below the skin surface, providing the potential for medical imaging, particularly, of epithelial tissues where most cancer originates. THz waves also offer a non-invasive imaging method as they do not damage human body like X-rays do [4].

Gas-phase detection has been a major application of Terahertz Time-Domain Spectroscopy (THz TDS). Early work includes the investigation of absorption, dispersion, and inversion spectrum of ammonia vapor $(NH_3)_2$ [5]. Terahertz spectroscopy was also used to investigate the laser induced ionization and plasma formation in pure oxygen and nitrogen to obtain the specifications of gases, such as the free electron density and the electron scattering time [6]. A long-baseline THz time domain spectrometer, capable of detecting gas species in the low part-per-million (PPM) range in near real-time, was reported [7]. This spectrometer was used to observe coherent transients from methyl chloride vapor directly in the time-domain. The analysis of chemical compositions is a fundamental issue in molecular spectroscopy. Studies of the coherent transient response of resonantly excited gases and gas mixtures can be accomplished by THz TDS. Coherent transient phenomena appear in the time-domain spectra as free induction decays described by fast oscillations with corresponding echoes occurring after impulse excitation. A time-domain chemical-recognition system to classify gases and analyze gas mixtures based on this method was presented [8]. The detection and identification of polar gases and gas mixtures based on THz TDS was presented for real-time spectroscopic measurements over a broad bandwidth up to several THz [9]. This has been realized to distinguish between CH_3CN and CD_3CN [9] and separately, NH_3 and H_2O [10].

Rotational transitions of light polar molecules and low frequency vibrational modes of large molecular systems can be probed by THz spectroscopy. As an atmospheric pollutant, small molecules like hydrogen sulphide (H_2S), OCS, formaldehyde (H_2CO), and ammonia (NH_3) possess intense transitions in the THz range, ideal for THz

spectroscopy [11]. Large amplitude motions of bio-molecules can also be examined in the THz domain with a highly sensitive spectrometer.

THz TDS also has several applications in the area of explosive detection. Especially in the gas-phase, flames, plumes, and explosive vapour are of great interest. Many explosives have unique spectral fingerprints in the THz range. The vapor-phase spectrum of DNT from 0.05 THz to 2.7 THz was reported utilizing pulsed THz TDS [12]. Combustion processes have attracted intensive investigation for commercial as well as scientific reasons. Of great importance are understanding and modeling of combustion, and that requires knowing the species present in the flame and the spatial distribution and temperature on these species. The first comprehensive THz absorption measurement of combustion products in a premixed laminar hydrocarbon-air flame was presented using THz TDS in [13]. A large number of absorption lines including those of water, CH, and NH_3 were observed. The flame temperature was also determined by comparison of the relative strength of the water vapour lines.

1.2 THz generation and detection

The objective of broadband THz generation and detection is to produce and probe an ultra-short electrical pulse with the duration within the ps range corresponding to a spectrum in the THz frequency range. There are methods to generate such pulses using only optical means (optical rectification), or using only electronic means (nonlinear transmission lines, resonant tunnelling diode, etc) [2]. However, in the most common generation method, the THz photoconductive antenna, mixed optical and electronic means are used to generate THz pulses. The photoconductive antenna is basically a small dipole antenna deposited on an ultra-fast substrate with less than 1 ps carrier lifetime. A fs pulse laser with photon energy greater than the substrate bandgap is focused on the antenna feed gap, exciting electron-hole pairs. The photo-excited carriers are accelerated by the bias voltage applied across the gap, yielding emission of a pulsed electromagnetic radiation with a bandwidth in the THz range.

THz detection is also a challenging task since THz sources are usually weak, and ambient thermal noise dominates over THz signals due to low photon energy of THz waves (4 meV). However, heterodyne detection used in terahertz time-domain

spectroscopy (THz TDS) can increase significantly signal-to-noise-ratio. In heterodyne detection methods, the same photoconductive antenna is used as a receiver. THz waves impinging on the receiver dipole antenna induce a pulsed voltage across the antenna gap. This voltage can be probed by measuring the receiver current when a fs optical pulse excites free carriers in the receiver gap.

1.3 THz waveguides

One important component for advancing optical and microwave systems is the use of waveguides for channeling electromagnetic fields. The existence of practical and low-loss waveguides like optical fibers, coaxial cables and planar transmission lines drove generations of high-speed communication systems. Terahertz systems, unfortunately, suffer from the lack of a low-loss well-behaved waveguide despite substantial research conducted on the subject.

Confining THz radiation within waveguide structures offers tremendous potential advantages in size, performance, and versatility, driving research on many types of THz waveguides. Using transmission lines and waveguides can help the integration of THz systems, avoiding the difficulties associated with THz beam-shaping and beam-steering optics.

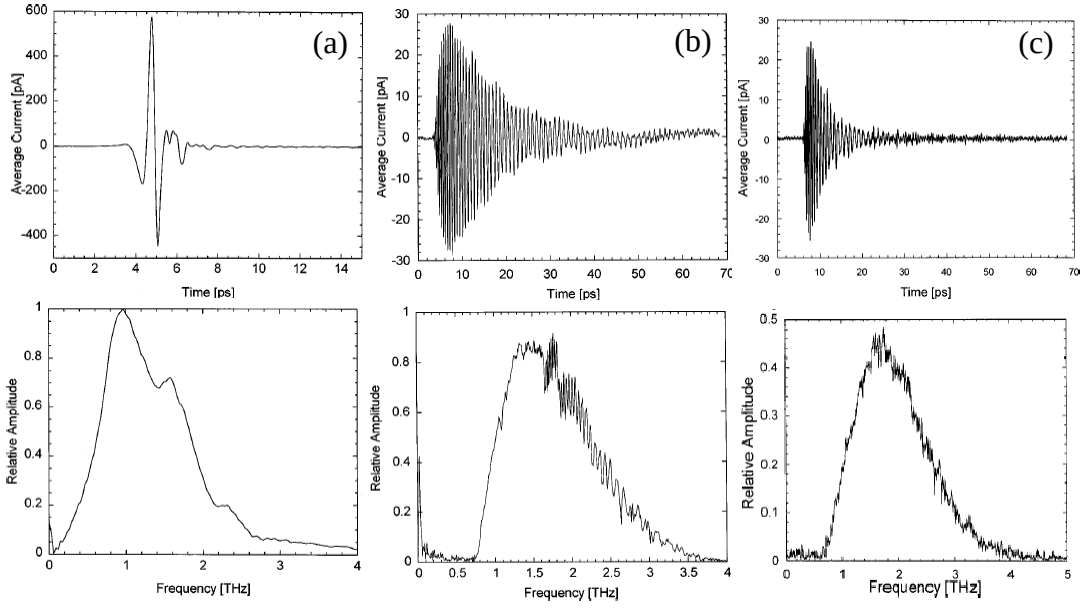

Figure 1.2 (a) THz pulse in time and frequency domain without waveguide, (b) THz pulse in time and frequency domain with the circular waveguide, (c) THz pulse in time and frequency domain with the rectangular waveguide [15].

Early terahertz waveguides include coplanar transmission lines, with an attenuation constant of 20 cm^{-1} [14]. Microwave metal-pipe waveguides can have lower loss (about 1 cm^{-1}) but they are highly dispersive due to the existence of cutoff frequencies for propagating modes, and multi-mode propagation limits usable bandwidth [15]. Test results for circular and rectangular waveguide, reported in [15], are illustrated in Fig. 1.2. Pulse stretching is evident for both cases due to the strong group-velocity dispersion of the waveguides. There is also a sharp cutoff frequency in the spectra due to the cutoff frequency of the first-order mode supported by the waveguides. The strange oscillations in the spectra are attributed to multi-mode propagation in the waveguides.

Waveguides fabricated with dielectrics like sapphire or high-density polyethylene (HDPE), which have low loss in the THz range, were reported with about 1 cm^{-1} loss [16,17]. Figure 1.3 shows a THz pulse transmitted through unclad sapphire fibers with different diameters as reported in [17]. There is significant pulse reshaping due to the strong group-velocity dispersion of the waveguide.

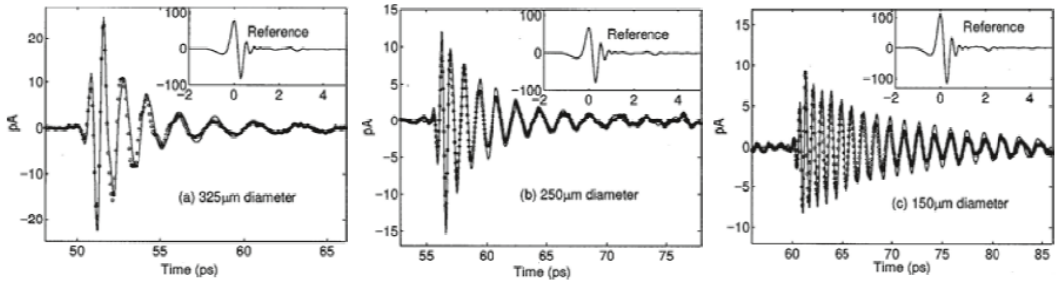

Figure 1.3 Measured and calculated terahertz pulse transmitted through sapphire fibers with 325μm, 250μm and 150μm diameter [17].

Supporting TEM modes, parallel-plate waveguides solve the problem of dispersion and have reasonably low loss (0.1 cm^{-1}) [18]. Dielectric fiber with sub-wavelength diameter for terahertz waveguiding has been demonstrated [19]. The sub-wavelength fiber was designed to carry most of the terahertz energy in the air surrounding the fiber. 0.01 cm^{-1} loss at 0.3THz and 20% coupling coefficient with a 200μm-diameter fiber made of polyethylene (PE) was reported. But waveguide and material dispersion limit the applicability of this waveguide for broadband applications. Also, this waveguide suffers

from large bend loss since electromagnetic energy is mostly extended in air surrounding the fiber.

With a similar motivation to carry a terahertz wave in air, a stainless steel bare metal wire shows less than 0.03 cm^{-1} absorption at 1 THz [20]. A fundamental challenge for the single metal wire waveguide is that it is difficult to couple the electromagnetic wave efficiently to the radially-polarized mode supported by this waveguide. In [20] the THz wave is scattered by another metal wire perpendicular to the first one, to couple to the surface mode supported by the waveguide. Fig. 1.4(a) shows the surface wave profile supported by the metal wire waveguide. The THz wave emitted from common dipole antennas is linearly-polarized and highly mismatched with the surface mode supported by the waveguide, resulting in poor coupling efficiency. Coupling efficiency less than 1% has been reported for the scattering coupling method [21]. Radially-symmetric photoconductive antennas, shown in Fig. 1.4(b), can significantly enhance the coupling efficiency but at the price of losing efficiency of the photoconductive generation process [21].

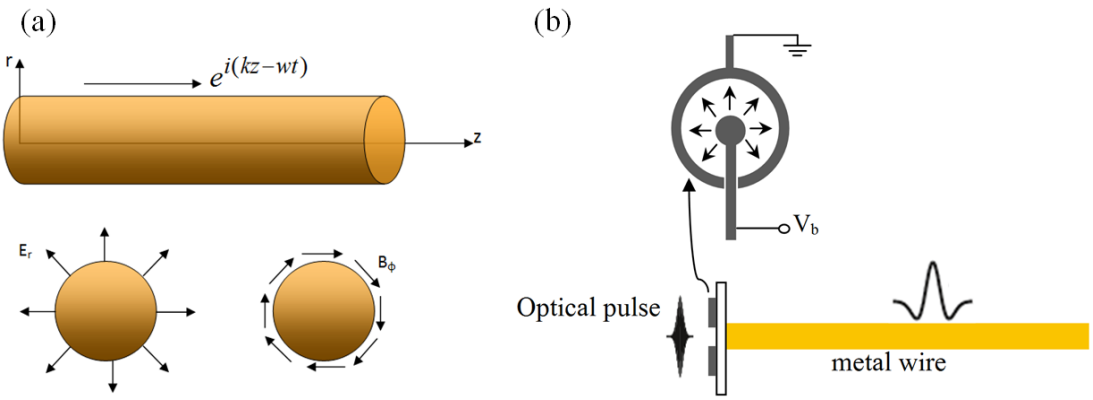

Figure 1.4 (a) The surface wave propagating on the metal wire, (b) coupling terahertz wave into the surface mode of the single wire by radially-symmetric photoconductor.

Two-wire waveguides [22,23] combine both low loss and efficient coupling properties. The field polarization of the TEM mode supported by this type of waveguide is very similar to the field emitted from a simple dipole, resulting in efficient coupling of the electromagnetic energy from typical terahertz sources into that mode. Also, for the TEM mode there is no cut-off frequency and no group velocity dispersion. Thus, one can enjoy the low loss of the wire waveguide along with dispersion-free propagation of the

TEM mode. Confining electromagnetic energy in a small area between the two wires is another important advantage of this waveguide that makes it more practical and more tolerant to bend loss [24]. Also, a wide variety of interesting choices and field configurations can be developed by simply varying the space between two wires, a degree of freedom unavailable to alternative waveguides.

Planar transmission lines like microstrips, coplanar striplines, and slot-lines have also been proposed to support terahertz waves [14,25,26]. They are compact and fairly easy-to-make, helping the integration of THz systems. Passive components like dividers/combiners and couplers can be realized using planar transmission lines. In the THz range, however, dispersion and loss limit the applicability of conventional transmission lines.

1.4 Scope of this thesis

In this dissertation, we first evaluate the performance of the two-wire waveguide theoretically and with numerical simulations in the THz frequency range in Chapter 2. In Chapter 3, we introduce and evaluate two novel planar transmission lines: slot-line in homogenous medium and slot-line on a layered substrate, capable of operating in the THz range without significant loss. Chapter 4 presents experimental results for the two-wire waveguide and the slot-line in GaAs. In Chapter 5, a tapered structure is introduced to couple efficiently THz waves from a source to a two-wire waveguide. We will show how we exploit both excellent coupling coefficient of the slot-line and low loss property of the two-wire waveguide in the tapered structure. Finally, Chapter 6 deals with an important application of the two-wire waveguide in realizing a THz cable.

Chapter 2

Two-Wire Waveguide for Terahertz Waves

It is anticipated that waveguides will form an important part of future THz systems. Using waveguides can be a way to avoid the alignment and loss challenges associated with the manipulation of THz waves by THz optics. Several microwave and optical waveguide structures have been used for THz applications like coplanar strip line (CPL), metal pipes, dielectric fibres, etc. But they have either high attenuation or high dispersion that prevents THz wave or pulse transmission over long distances. In this chapter, we introduce the two-wire waveguide as a low-loss, non-dispersive waveguide for THz waves. Rigorous theoretical analysis of the two-wire THz waveguide is presented for evaluating absorption and coupling coefficient in terms of the dimensions of the waveguide. Theoretical results are validated by numerical simulations.

2.1 TEM mode

Obtaining field distributions for the two-wire waveguide calls for solving Maxwell's equations with the boundary conditions forced by the structure of the waveguide. We developed a mapping function for solving this problem [23], similar to the method described in [27]. As mentioned before, the two-wire waveguide can support a TEM mode as well as TE and TM modes. The Helmholtz wave equation for the electric field is

$$\nabla^2 \vec{E} + k^2 \vec{E} = 0, \tag{2.1}$$

$$k = \omega\sqrt{\mu\varepsilon}\,.$$

For a wave propagating in the *z*-direction with $e^{-i\beta z}$ dependence, the wave equation reduces to

$$(\nabla_t^{\,2} + k_c^{\,2})\vec{E}_t = 0, \tag{2.2}$$

where,

$$\nabla_t = \partial^2/\partial x^2 + \partial^2/\partial y^2,\ \vec{E}_t = E_x \hat{x} + E_y \hat{y},\ k_c = \sqrt{k^2 - \beta^2}\,.$$

For the TEM mode, the problem of obtaining fields outside the conductors reduces from the wave equation to the 2D Laplace equation, a considerable simplification, because $k_c=0$. Indeed, the transverse fields of the TEM mode are the same as the static fields between the conductors. One powerful mathematical method for solving the 2D Laplace equation is conformal mapping based on the properties of harmonic functions [28]. In this method, a complicated geometry is mapped to a simpler one through a complex analytic function. The Laplace equation is solved in the simpler region and the solution is transformed to the original geometry.

The following two functions map the cross section of the two-wire waveguide to two concentric circles like the cross section of a coaxial cable as shown in Fig. 2.1.

$$f_1(z)=\frac{R}{z+D}, \tag{2.3}$$

$$f_2(z)=\frac{z-C_1}{C_2-z}, \tag{2.4}$$

$$C_1,C_2=\frac{D}{2R}\mp\sqrt{\left(\frac{D}{2R}\right)^2-1}\ . \tag{2.5}$$

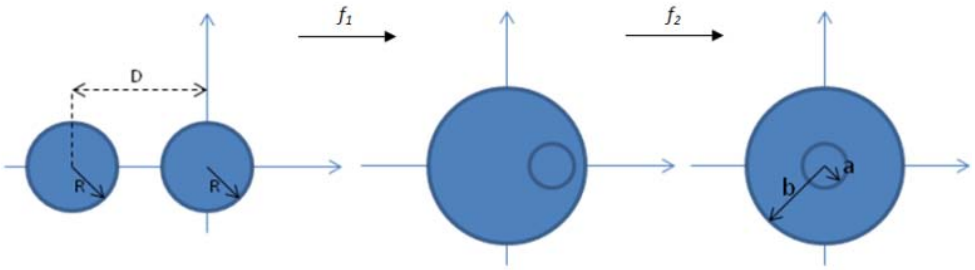

Figure 2.1 Conformal mapping of the cross section of two-wire waveguide to two concentric circles.

The potential function in the region between the two concentric circles is

$$V=V_0\frac{\ln(b/|z|)}{\ln(b/a)}, \tag{2.6}$$

where a and b are the radius of inner and outer circles, respectively:

$$a=\frac{1-C_1(D/R-1)}{C_2(D/R-1)-1},$$

$$b=\frac{1-C_1}{C_2-1}.$$

Substituting z in the potential according to the mapping functions results in having the potential in the desired region, namely the cross section of the two-wire waveguide. The electric field can be derived from the gradient of the potential:

$$\vec{E} = -\nabla V \,, \tag{2.7}$$

that, with some algebraic simplifications, yields

$$E_x = \begin{cases} \dfrac{V_0}{\ln(b/a)}\left[\dfrac{(x+R/C_2)}{(x+R/C_2)^2+y^2} - \dfrac{(x+R/C_1)}{(x+R/C_1)^2+y^2}\right] & \text{outside the wires} \\ 0 & \text{inside the wires} \end{cases}, \tag{2.8}$$

$$E_y = \begin{cases} \dfrac{V_0}{\ln(b/a)}\left[\dfrac{y}{(x+R/C_2)^2+y^2} - \dfrac{y}{(x+R/C_1)^2+y^2}\right] & \text{outside the wires} \\ 0 & \text{inside the wires} \end{cases}. \tag{2.9}$$

Figure 2.2 shows the distribution of the amplitude of the electric field in the cross section of the two-wire waveguide obtained from the theoretical analysis. The field distribution is consistent with the simulation results reported in [22].

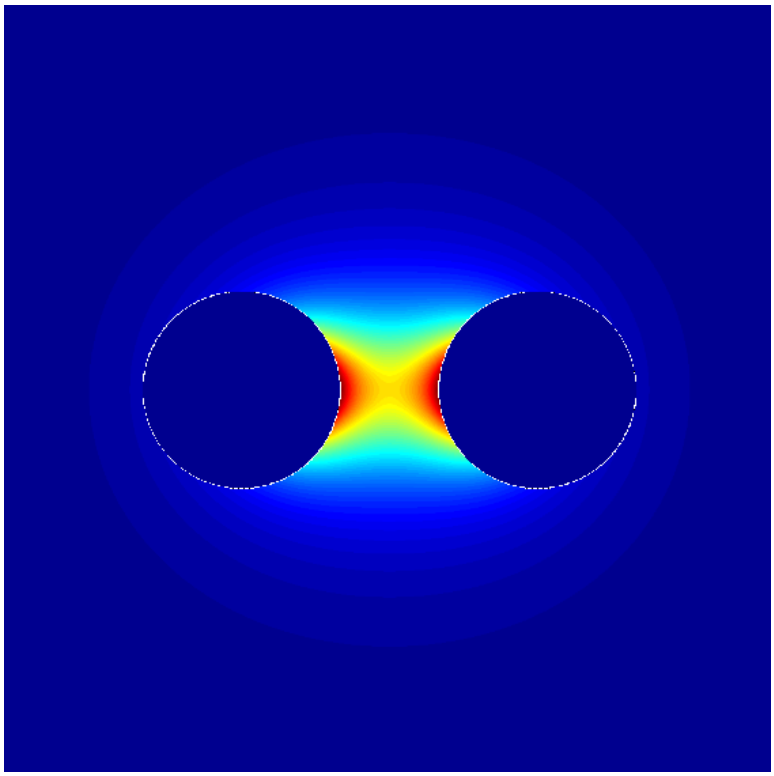

Figure 2.2 Electric field distribution of the TEM mode supported by two-wire waveguide.

Figure 2.3 also compares the electric field amplitude in the *x*-axis (Y = 0) between the two wires obtained from the theory with our numerical simulation results using Ansoft HFSS solver at 1 THz. It is quite clear that the results are in good agreement, confirming the validity of our theory.

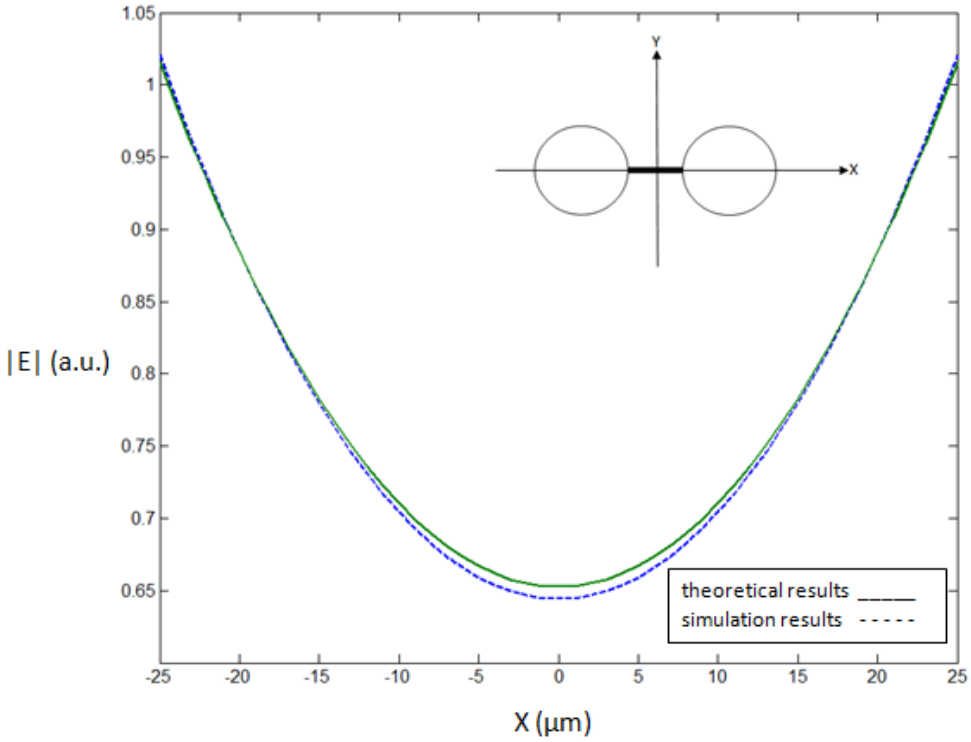

Figure 2.3 Electric field in the *x*-axis obtained from the theory (solid line) and our numerical simulations (dashed line).

Figure 2.4 shows the field distribution for different values of the wire centre-to-centre distance *D*. The figure illustrates the wide variation in field distribution with change in *D*. When the wires are close, the field concentrates in the gap between the wires. When the wires are distant, the field more evenly surrounds the wires. Therefore, we expect that conductor loss would be lower for larger distances between the wires since the current produced by the field in the wires passes a larger cross section area when the field is more distributed, reducing the effective resistivity. However, moving the wires farther apart allows the waveguide to support higher-order modes. Multi-mode propagation is not desirable for broadband applications as it distorts the spectrum of the THz pulse after propagation along the waveguide. Numerical simulations can be used to determine cutoff frequencies of higher-order modes for different dimensions of the waveguide. Also, a

lower center-to-center distance of the wires results in a more confined field, leading to smaller bend loss and radiation loss. These factors limit the maximum value of *D*. We anticipate that this dependence of field strength on *D* can form the basis of future interesting sensor devices. The radius of the wires also has a large impact on the field distribution. As the radius *R* increases, the field is distributed over a larger area, suggesting lower conductor loss for bigger wires.

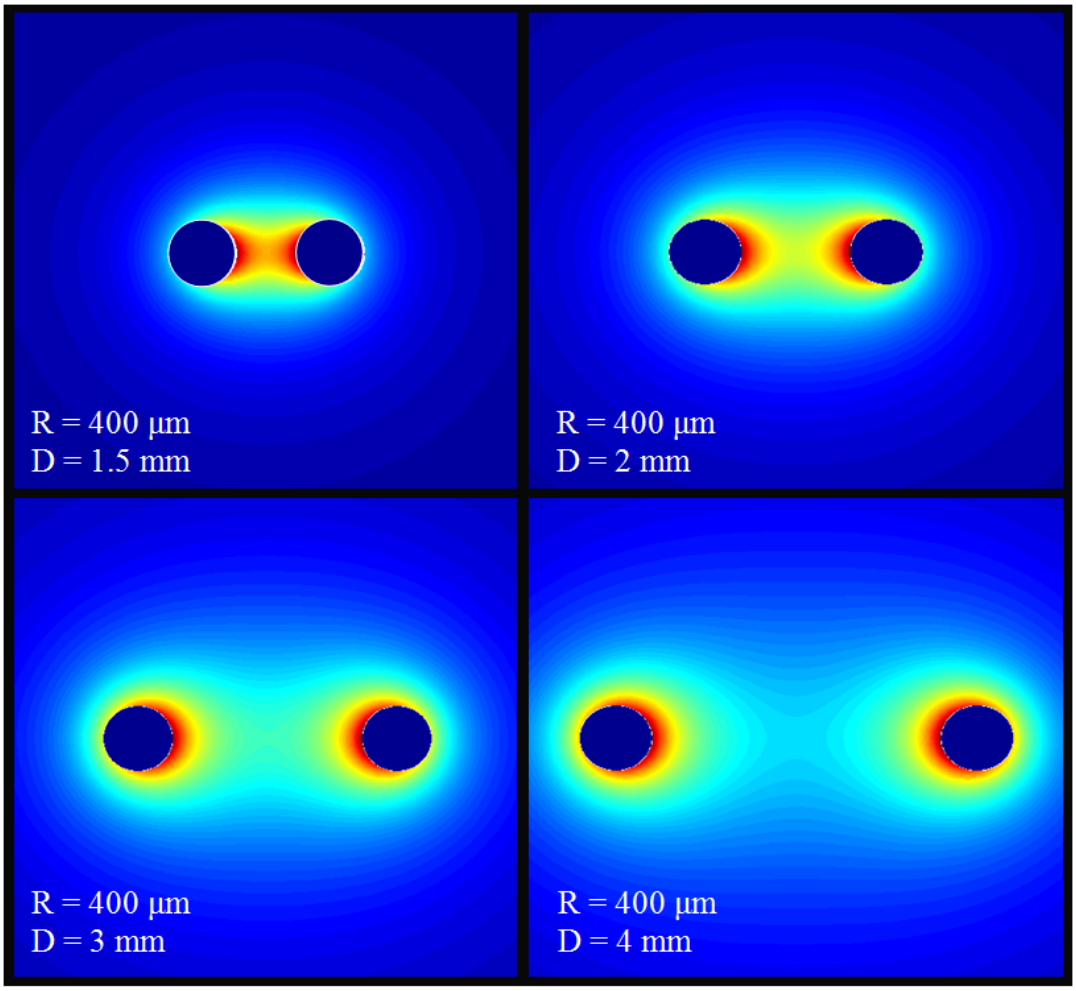

Figure 2.4 Electric field distribution for different values of *D*.

2.2 Loss estimation

One important property of a waveguide working in the THz frequency range is having low absorption. Since available THz sources are usually weak, it is important to avoid any loss in delivering THz signals from the emitter to the receiver. For the two-wire waveguide in free space, conductor loss is the only absorption mechanism as the

propagation medium, free space, does not have dielectric loss. In this section, we estimate the conductor loss of the two-wire waveguide in terms of the dimensions using analytic expressions we derived in the previous section for the potential function and the field of the TEM mode supported by the waveguide.

In a perfect conductor, the surface charge density should be

$$\rho_s = \hat{n} \cdot \vec{D} \tag{2.10}$$

to give zero electric field inside the perfect conductor. The movement of electric charges also produces a surface current

$$\vec{J}_s = \hat{n} \times \vec{H} \tag{2.11}$$

to give zero magnetic field inside the perfect conductor. Therefore, just outside a perfect conductor there are only normal electric field and tangential magnetic field. A good, but not perfect, conductor must exhibit approximately the same behavior. In [29], it is shown that the fields inside a good conductor are

$$\vec{H}_c = H_{\|} e^{-\xi/\delta} e^{i\xi/\delta}, \tag{2.12}$$

$$\vec{E}_c \cong \sqrt{\frac{\mu\omega}{2\sigma}}(1-i)\left(\vec{n} \times \vec{H}_{\|}\right) e^{-\xi/\delta} e^{i\xi/\delta}, \tag{2.13}$$

$$\delta = \sqrt{\frac{2}{\omega\mu\sigma}}, \tag{2.14}$$

where ξ is the normal coordinate inward into the conductor, $H_{||}$ is the tangential magnetic field outside the surface, E_c and H_c are the electric and magnetic field inside the conductor, μ is the permeability of the conductor, δ is the skin depth (Eq. 2.14) and σ is the conductivity. Accordingly, the time-averaged power absorbed per unit area is

$$\frac{dP_{loss}}{dA} = \frac{\mu\omega\delta}{4} |\vec{H}_{\|}|^2, \tag{2.15}$$

where A is the surface area of the conductor. Eq. 2.15 shows how the conductor loss changes with the frequency (or wavelength) and with the material of the conductor through the skin depth. To estimate the waveguide loss, Eq. 2.15 suggests that we must obtain the tangential magnetic field just above the metal surface.

For the TEM mode, the magnetic field can be derived easily from the electric field with the following relationships:

$$\frac{E_x}{H_y} = \eta_0, \tag{2.16}$$

$$\frac{-E_y}{H_x} = \eta_0, \tag{2.17}$$

where η_0 is the intrinsic impedance of free space. Knowing the magnetic field just outside the surface of the conductor allows us to estimate the power loss per unit length of the waveguide according to

$$P_{loss} = \frac{\mu\omega\delta}{4}\int_S \left|\vec{H}_{\parallel}\right|^2 ds, \tag{2.18}$$

where *ds* is the infinitesimal surface element of the conductor. Note that there is no attenuation due to dielectric loss because the two wires are surrounded by air. Another necessary parameter for determining attenuation constant is P_0, the power flowing on the lossless line:

$$P_0 = \frac{1}{2}\Re\left\{\int_{S'}\left(\vec{E}\times\vec{H}^*\right)\cdot d\vec{s}\right\}, \tag{2.19}$$

where S' is the surface element of the cross section of the waveguide. Calculation of P_0 includes a complicated surface integral on the cross section of the two-wire waveguide. The following theorem may be used to simplify the integration.

Theorem: Suppose the potential function Φ is transferred from the *xy*-plane to the *uv*-plane by an analytical complex function. The energy stored in the fields, calculated in both planes is the same [30]:

$$\iint_{xy}\left[\left(\frac{\partial\Phi}{\partial x}\right)^2+\left(\frac{\partial\Phi}{\partial y}\right)^2\right]dxdy = \iint_{uv}\left[\left(\frac{\partial\Phi}{\partial u}\right)^2+\left(\frac{\partial\Phi}{\partial v}\right)^2\right]dudv\,. \tag{2.20}$$

Therefore, the integration can be calculated on the simpler plane, namely the two concentric circles shown in Fig. 2.1 that yields

$$P_0 = \frac{\pi {V_0}^2}{\eta_0 \ln(b/a)}\,. \tag{2.21}$$

The attenuation constant is then

$$\alpha = \frac{P_l}{2P_0} = \frac{P_{loss}/L}{2P_0}, \tag{2.22}$$

where P_l is the power loss per unit length and L is the length of the waveguide. Substituting P_l and P_0 into Eq. 2.22 with some algebraic simplifications results in:

$$\alpha_c = \frac{\mu\omega\delta}{2\eta} \cdot \frac{1+C_1^{\,2}}{R\left(1-C_1^{\,2}\right)\ln\left(\frac{(D/R-1)-C_1}{1-C_1(D/R-1)}\right)}. \tag{2.23}$$

Figure 2.5 illustrates the dependence of the attenuation constant on D, the distance between the wires, and R, the radius of the wires, at 1THz for a waveguide made out of gold. The attenuation constant decreases as D becomes larger, consistent with the conclusion we derived from the field distribution. Increasing R also results in a smaller attenuation constant, also inferred from the field distribution. All the curves corresponding to the different values of R show similar behavior, i.e. decreasing loss with increasing D. There is also a knee in each curve that corresponds to an appropriate value for D, because further increase in D would not reduce absorption considerably. A closer look at the difference between the curves shows that increasing R more than 300μm does not change the loss significantly. Therefore, this value is probably a good choice for R for a wide range of applications.

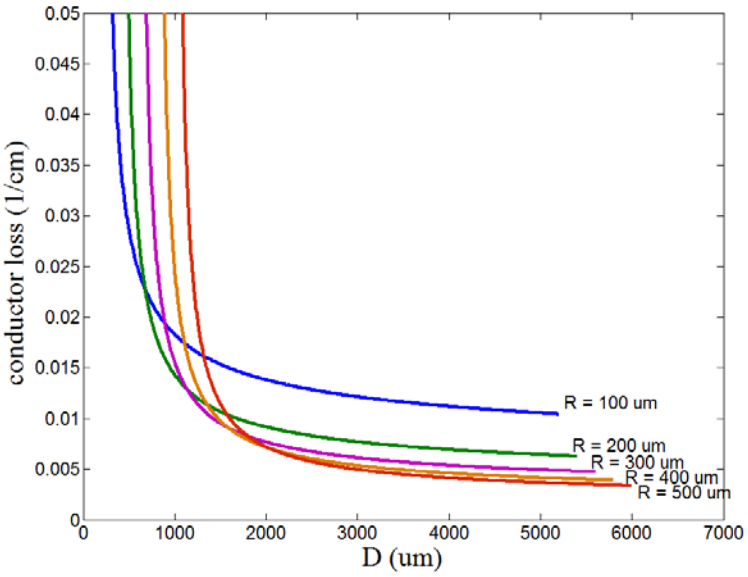

Figure 2.5 Two-wire waveguide conductor loss vs. center-to-center distance of the wires for 100 μm to 600 μm radii of the wires.

2.3 Coupling efficiency

Dipole antennas are used widely in terahertz photoconductive sources [31–33]. The radiation pattern of a dipole on a dielectric substrate has been investigated in detail in [34–38]. Inside the substrate, the terahertz wave is like a spherical wave. A silicon lens transforms this spherical wave approximately to a plane wave [39]. Coupling efficiency determines how much power can be coupled from the dipole source to the two-wire waveguide. Calculating the coupling efficiency is, in general, not a trivial problem, especially for a complicated structure like the dipole and the two-wire waveguide. However, given [39], we make the assumption that the far-field radiation of the dipole on the substrate can be approximated by a plane wave in the plane perpendicular to the dipole. This approach assumes that a plane wave with certain dimensions (depending on the directivity of the source) impinges on the input port of the waveguide. This approximation is valid when the waveguide cross section is comparable to or smaller than the far-field radiation pattern of the dipole, which is the case for a typical terahertz source [39–41].

A second approximation replaces the radiated plane wave with certain dimensions at the input port of the two-wire waveguide by the TEM mode of a fictitious parallel-plate waveguide of the same dimensions, as shown in Fig. 2.6. If the plane wave is a good approximation for the incident THz wave, the field incident on the two-wire waveguide is the same whether the incident wave is a plane wave or the TEM mode of a parallel-plate waveguide with the same dimensions. What matters in coupling to the two-wire waveguide is the distribution of the field at its input port, which is identical for both cases. This approximation enables us to use a simple mode-matching technique to calculate the coupling efficiency from the TEM mode of a parallel-plate waveguide into the TEM mode of a two-wire waveguide.

We assume that the TEM mode of a parallel-plate waveguide (with the cross section of $w \times d$ and with 1W power) corresponding to a plane wave, impinges on the input port of a two-wire waveguide. The coupling efficiency is the ratio of the transmitted power to the incident power [15].

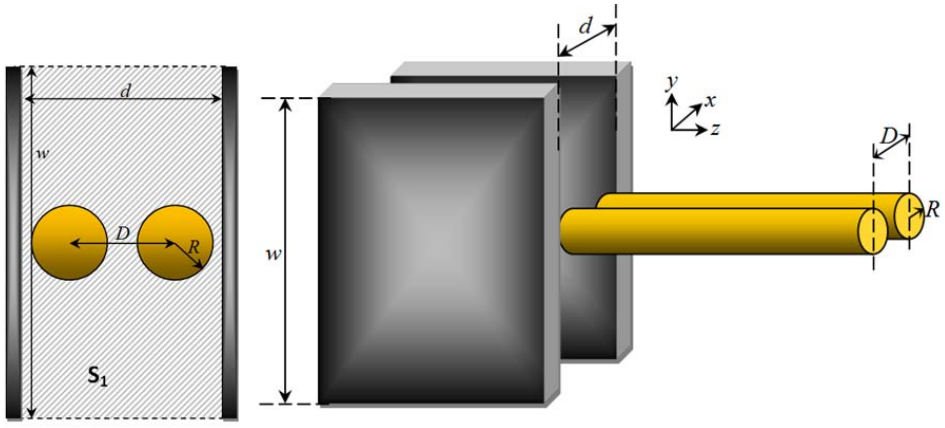

Figure 2.6 Intersection of the parallel-plate waveguide and the two-wire waveguide.

The physical modes supported by the waveguides form a complete, orthogonal basic set; therefore, the fields can be expressed in terms of the modes on both sides [29,42]:

$$\vec{E}_{1,2} = \sum_m \left(a_{1,2m} + b_{1,2m}\right)\vec{e}_{1,2m}\,, \tag{2.24}$$

$$\vec{H}_{1,2} = \sum_m \left(a_{1,2m} - b_{1,2m}\right)\vec{h}_{1,2m}\,, \tag{2.25}$$

where E, H are the electric and magnetic field, a_m, b_m are the coefficients for forward and backward waves, e_m, h_m are the normalized electric and magnetic fields of the mth mode, and subscripts *1*, *2* are for the parallel-plate waveguide and the two-wire waveguide, respectively. The orthonormalization of the modes can be written [42]

$$\frac{1}{2}\iint\left(\vec{e}_l \times \vec{h}_m^{\,*}\right)\cdot\hat{z}\,ds = \delta_{lm}\,, \tag{2.26}$$

where l, m are the mode subscripts, and δ_{lm} is the Kronecker delta. The boundary conditions at the interface of the two waveguides require:

$$\vec{E}_{t1}\left(z=0^-\right) = \vec{E}_{t2}\left(z=0^+\right), \tag{2.27}$$

$$\vec{H}_{t1}\left(z=0^-\right) = \vec{H}_{t2}\left(z=0^+\right), \tag{2.28}$$

where the subscript t indicates the transverse components of the fields. The single lowest-order TEM mode is incident from the left side. Continuity of the transverse electric field expanded in terms of the orthogonal modes on both sides gives:

$$(1+r)(\vec{e}_1)_{TEM} + \sum_{m=2}^{\infty} b_{1m}\vec{e}_{1m} = t(\vec{e}_2)_{TEM} + \sum_{m=2}^{\infty} a_{2m}\vec{e}_{2m}\,, \tag{2.29}$$

where *r*, *t* are the reflection and transmission coefficients, respectively. Multiplying both sides of Eq. 2.28 by $1/2(h_1)_{TEM}^{*}$, integrating over the transverse plane (XY-plane), and using orthoganality relations for the parallel-plate waveguide modes yields

$$(1+r) = (t)\kappa + \frac{1}{2}\sum_{m=2}^{\infty} a_{2m}\iint\left(\vec{e}_{2m}\times\vec{h}_{1TEM}^{\,*}\right)\cdot\vec{dS}\,, \tag{2.30}$$

where,

$$\kappa = \frac{1}{2}\iint\left(\vec{e}_{2TEM}\times\vec{h}_{1TEM}^{\,*}\right)\cdot\vec{dS}\,. \tag{2.31}$$

Similarly, continuity of the transverse magnetic field expanded in terms of the orthogonal modes on both sides gives

$$(1-r)(\vec{h}_1)_{TEM} + \sum_{m=2}^{\infty}(-b_{1m})\vec{h}_{1m} = t(\vec{h}_2)_{TEM} + \sum_{m=2}^{\infty} a_{2m}\vec{h}_{2m}\,. \tag{2.32}$$

multiplying both sides of Eq. 2.32 by $1/2(e_2)_{TEM}^{*}$, integrating over the transverse plane, and using the orthogonality relations for the two-wire waveguide modes yields

$$(1-r)\kappa + \frac{1}{2}\sum_{m=2}^{\infty}(-b_{1m})\iint\left(\vec{e}_{2m}\times\vec{h}_{1TEM}^{\,*}\right)\cdot\vec{dS} = t\,. \tag{2.33}$$

Neglecting the effects of the higher order modes results in simple relations for the transmission and reflection coefficients:

$$|r|^2 = \left(\frac{\kappa^2-1}{\kappa^2+1}\right)^2, \tag{2.34}$$

$$|t|^2 = \left(\frac{2\kappa}{\kappa^2+1}\right)^2. \tag{2.35}$$

Therefore, reflection and transmission coefficients can be obtained by calculating κ.

According to the Eq. 2.31, calculation of κ calls for knowing the electric and magnetic fields of the TEM mode for the two waveguides. The TEM mode for the parallel-plate waveguide is [43]:

$$(\vec{e}_1)_{TEM} = \begin{cases} -A_1 \hat{x} & \text{between the plates} \\ 0 & \text{otherwise} \end{cases}, \tag{2.36}$$

$$(\vec{h}_1)_{TEM} = -\frac{|\vec{e}_1|}{\eta_0} \hat{y}, \tag{2.37}$$

where η_0 is the intrinsic impedance of free space and A_1 is the normalization constant that is chosen so that the TEM mode carries 1 W,

$$A_1^2 = \frac{2\eta_0}{wd}, \tag{2.38}$$

where w are the width of the plates, and d is the distance between the plates. Explained in Section 2.1, the TEM mode for the two-wire waveguide is [23]

$$(\vec{e}_2)_{TEM} = e_{2x} \hat{x} + e_{2y} \hat{y}, \tag{2.39}$$

$$(\vec{h}2)_{TEM} = \frac{1}{\eta_0} \hat{z} \times (\vec{e}_2)_{TEM} = \frac{1}{\eta_0} \left(e_{2x} \hat{y} - e_{2y} \hat{x} \right), \tag{2.40}$$

where, e_{2x} and e_{2y} can be obtained from Eq. 2.8 and Eq. 2.9, respectively. A_2 is the normalization constant that can be obtained from the equation below,

$$\frac{1}{2\eta_0} \iint \left(|e_{2x}|^2 + |e_{2y}|^2 \right) dxdy = 1, \tag{2.41}$$

that yields

$$A_1 = \sqrt{\frac{2\eta_0}{2\pi \ln(b/a)}}. \tag{2.42}$$

Substituting the fields in Eq. 2.31 yields

$$\kappa = \frac{A_1 A_2}{2\eta_0} \iint_{S_1} \left[\frac{(x + R/C_2)}{(x + R/C_2)^2 + y^2} - \frac{(x + R/C_1)}{(x + R/C_1)^2 + y^2} \right] ds, \tag{2.43}$$

where S_1 is the surface specified with the pattern in Figure 2.6. Green's theorem makes the surface integration in Eq. 2.43 significantly easier.

Green's Theorem: Let F_1 and F_2 be continuous differentiable functions on a simply connected domain D, and let Γ be a positively oriented simple closed contour around D. Then Eq. 2.44 is valid:

$$\int_{\Gamma} (F_1 dx + F_2 dy) = \iint_D \left(\frac{\partial F_2}{\partial x} - \frac{\partial F_1}{\partial y} \right) dxdy. \tag{2.44}$$

Eq. 2.6 and Eq. 2.7 show that the electric field is

$$\vec{e_2} = A_2 \nabla_t \left(\ln\left(|z_2| \right) \right) = A_2 \left(\frac{\partial}{\partial x} \left(\ln\left(|z_2| \right) \right) \hat{x} + \frac{\partial}{\partial y} \left(\ln\left(|z_2| \right) \right) \hat{y} \right), \tag{2.45}$$

where z_2 is the complex variable in the region between the two concentric circles in Figure 2.1, and can be expressed in terms of x ,y by

$$|z_2| = \sqrt{\frac{[R - C_1(x + D)]^2 + (C_1 y)^2}{[R - C_2(x + D)]^2 + (C_2 y)^2}} \,. \tag{2.46}$$

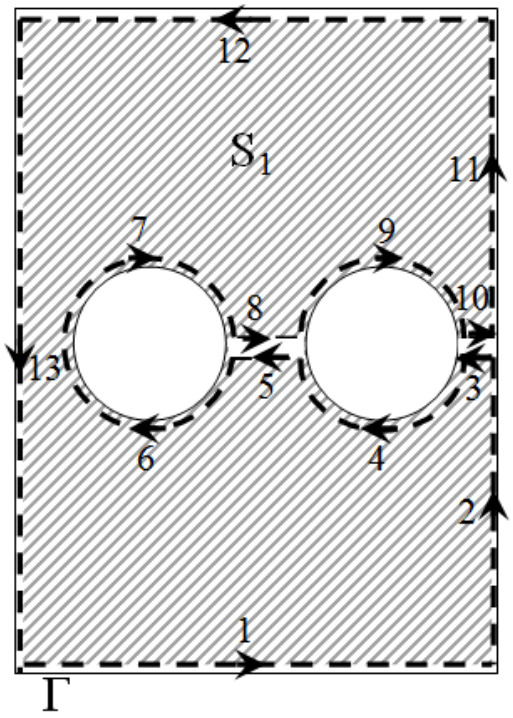

Figure 2.7 Integration contour for coupling.

Substituting the x component of the electric field in Eq. 2.31 and using Green's theorem yields

$$\kappa = -\frac{A_1 A_2}{2\eta_0} \iint_{S_1} \frac{\partial}{\partial x} \left[\ln\left(|z_3| \right) \right] dx dy = -\frac{A_1 A_2}{2\eta_0} \int_{\Gamma} \ln\left(|z_3| \right) dy \,, \tag{2.47}$$

where the surface S_1 and the contour Γ are shown in Figure 2.7. The integrations on the routes 1 and 2 are zero because y is constant. So are the integrations on the routes 3 to 10 because the integrand is the even function of y. Thus, the calculation of κ reduces to the integrations on the routes 2, 11 and 13 that yield

$$\kappa = \frac{A_1 A_2}{2\eta_0}\left\{ w \ln\left[\frac{\left(\frac{d-D}{2}+\frac{R}{C_1}\right)^2+\left(\frac{w}{2}\right)^2}{\left(\frac{d-D}{2}+\frac{R}{C_2}\right)^2+\left(\frac{w}{2}\right)^2} \right] + 4\left(\frac{d-D}{2}+\frac{R}{C_1}\right)\tan^{-1}\left(\frac{w/2}{\frac{d-D}{2}+\frac{R}{C_1}}\right) - 4\left(\frac{d-D}{2}+\frac{R}{C_2}\right)\tan^{-1}\left(\frac{w/2}{\frac{d-D}{2}+\frac{R}{C_2}}\right) \right\}. \tag{2.48}$$

Note that Eq. 2.31 is valid provided the cross section of the parallel-plate waveguide is larger than the one for the two-wire waveguide. This method can be applied to the other cases as well. Figure 2.8(b) shows the contour for the case that the separation of the parallel plates is smaller than the edge-to-edge distance of the wires. The integrations on routes 2 and 4 are zero because y is constant. So the calculation of κ reduces to the integrations on routes 1 and 3 that result in the same equation as Eq. 2.31. However, the case shown in Fig. 2.8(a) results in a different relationship for κ. The integrations over 1 and 6 are zero because y is constant, and so are the integrations on routes 3, 4, 8, and 9 because the integrand is the even function of y. Therefore, the calculation of κ reduces to the integrations on routes 2, 5, 7, and 10 that yields

$$\kappa = \frac{A_1 A_2}{2\eta_0}\left[w \ln\left[\frac{\left(\frac{d-D}{2}+\frac{R}{C_1}\right)^2+\left(\frac{w}{2}\right)^2}{\left(\frac{d-D}{2}+\frac{R}{C_2}\right)^2+\left(\frac{w}{2}\right)^2} \right] - 2\sqrt{R^2-\left(\frac{d-D}{2}\right)^2}\ln\left(\frac{\left(\frac{d-D}{2}+\frac{R}{C_1}\right)^2+R^2-\left(\frac{d-D}{2}\right)^2}{\left(\frac{d-D}{2}+\frac{R}{C_2}\right)^2+R^2-\left(\frac{d-D}{2}\right)^2} \right) \right.$$
$$\left. + 4\left(\frac{d-D}{2}+\frac{R}{C_1}\right)\tan^{-1}\left(\frac{w/2}{\frac{d-D}{2}+\frac{R}{C_1}}\right) - 4\left(\frac{d-D}{2}+\frac{R}{C_2}\right)\tan^{-1}\left(\frac{w/2}{\frac{d-D}{2}+\frac{R}{C_2}}\right) \right]. \tag{2.49}$$

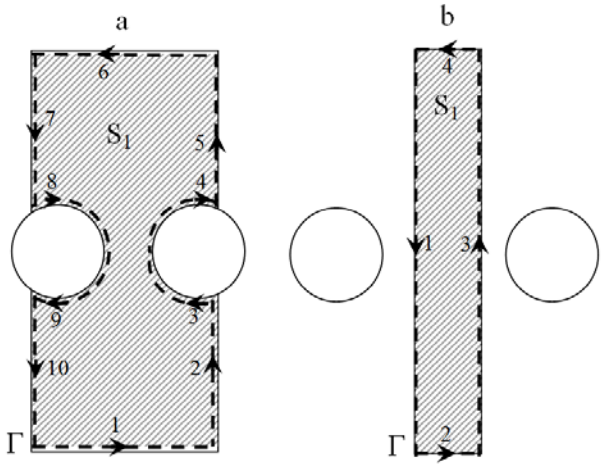

Figure 2.8 (a) Integration contour when D - 2R < d < D + 2R, (b) when d < D - 2R.

To verify the method, we first consider the case where the edge-to-edge distance of the two wires is kept constant and equal to the parallel-plate separation. As shown in Fig. 2.9(a), if the radii of the wires increase, the two-wire waveguide becomes more like the parallel-plate waveguide. Obviously, this change should lead to higher transmission and lower reflection coefficients. Figure 2.9(b) shows the transmission and reflection coefficients of the power ($|t|^2$, $|r|^2$) versus R, obtained from the proposed method for the same situation. They show the expected behavior, consistent with the intuitive conclusion.

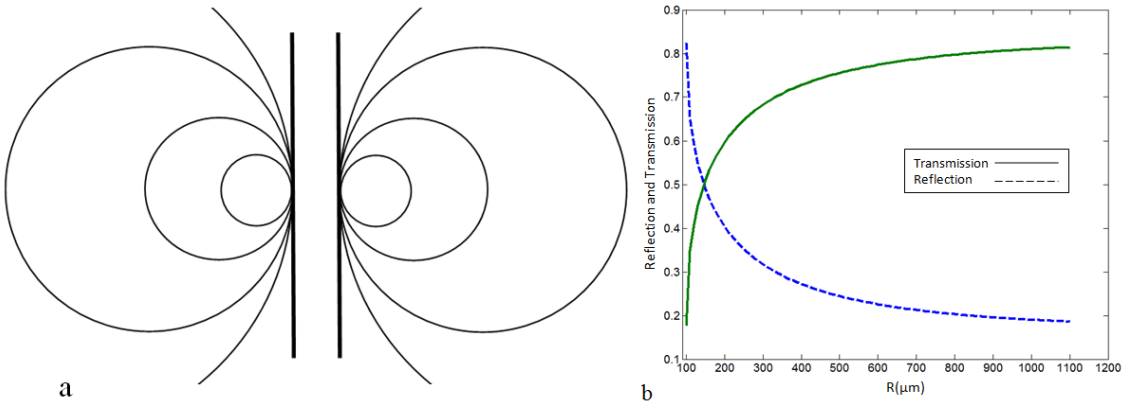

Figure 2.9 (a) Cross section of the two-wire waveguides with the same edge-to-edge wires' distance but different R, (b) the transmission and reflection coefficients.

Ideally, theoretical predictions would be validated experimentally. However, there are significant difficulties associated with the experimental measurement of the coupling. For instance, the absolute value of the radiated power from the source is difficult to measure. Also, other properties of the waveguide, like attenuation, vary with the change in the geometry of the waveguide, making it difficult to distinguish the impact of changes in each property. So we present numerical simulations to confirm the theoretical results.

We compare the coupling obtained from theory with results from 3D, full-wave simulations with the Finite Element Method (FEM) using the Ansoft HFSS frequency-domain solver. The simulations are applied to two-wire waveguides made out of gold with constant center-to-center distance of 400μm and different radii of the wires. Two cases are considered, both at 1THz. First, the waveguide is excited by a 0.5mm-long parallel-plate waveguide with 1mm × 0.4mm cross section, as shown in Fig. 2.10(a). Second, the waveguide is excited by a dipole, as shown in Figure 2.10(b). The

simulations are bounded by a rectangular box with 1mm × 1mm × 2mm size with radiation boundaries assigned to the walls of the box to avoid reflection. Only the TEM mode of the parallel-plate waveguide is excited in x-direction, using a wave port as the input port of the parallel-plate waveguide. For the dipole case, the distance between the dipole source and the input port of the two-wire waveguide is 200 μm and the direction of the dipole is in x-direction.

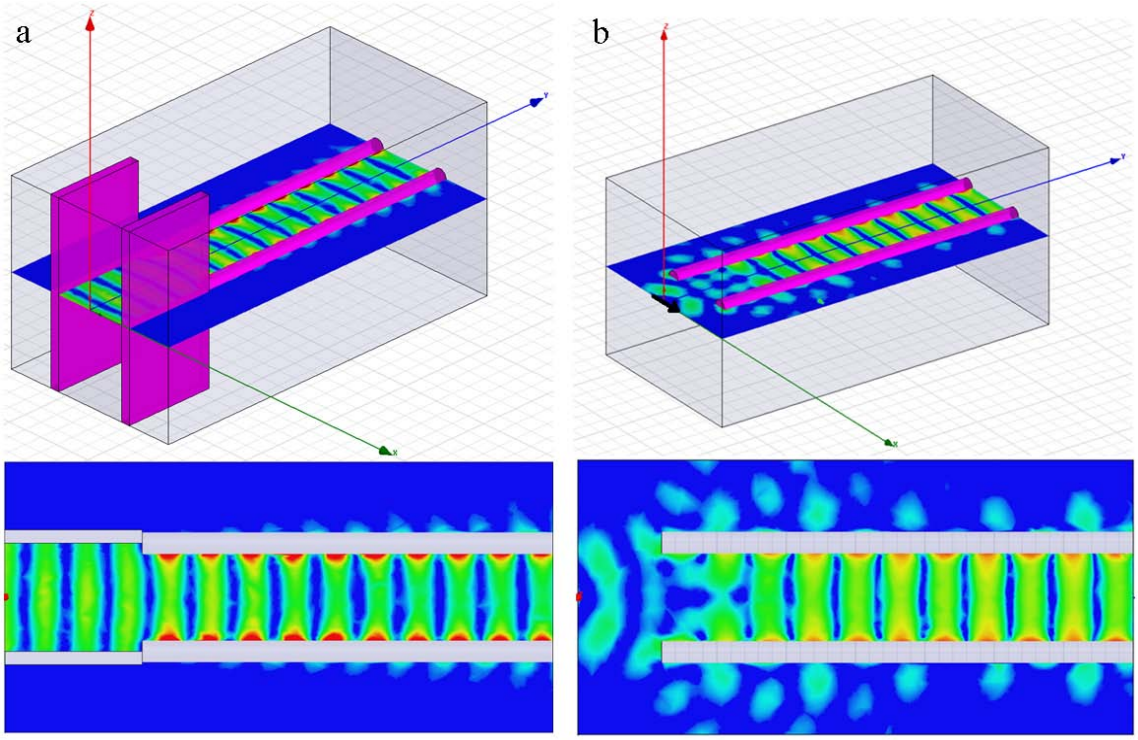

Figure 2.10 The amplitude of the electric field obtained from 3D full-wave simulations with FEM using Ansoft HFSS excited by (a) a 0.5mm-long parallel-plate waveguide with 1mm × 0.4mm cross section, (b) a dipole, 200 μm away from the input port of the two-wire waveguide, at 1THz .

To make a correct comparison between the results from the theory and the simulations, the incident power at the input port of the two-wire waveguide should be the same for both cases (theory and simulations), so we first measure numerically the power after the 0.5 mm-long parallel-plate waveguide and also the radiating power of the dipole at 200 μm away from the source, in the absence of the two-wire waveguide, using the Field Calculator of HFSS. Then we normalize all the measured power to those values so that we have the same input power to the two-wire waveguide in each case (1W). Then, the coupling efficiency is the normalized power measured at the output port of the two-

wire waveguide. Note that at the input port of the waveguide, many modes, both propagating and evanescent, must be superposed in order to keep the boundary conditions satisfied. This is responsible for the peculiar shape of the field near the input of the waveguide that is conspicuous in Figure 2.10(b). Far away from the input port, however, the field is relatively simple, with only the TEM mode (provided the dimensions of the waveguide allow just single-mode propagation) propagating with appreciable amplitude. The cutoff modes have considerable amplitude just near the input port and they fade over distances [29]. We also choose the length of the two-wire waveguide to be small enough that the waveguide loss is negligible and does not affect the coupling. As a result of these considerations, the measured normalized power at the output port appears to provide a legitimate value for the coupling efficiency.

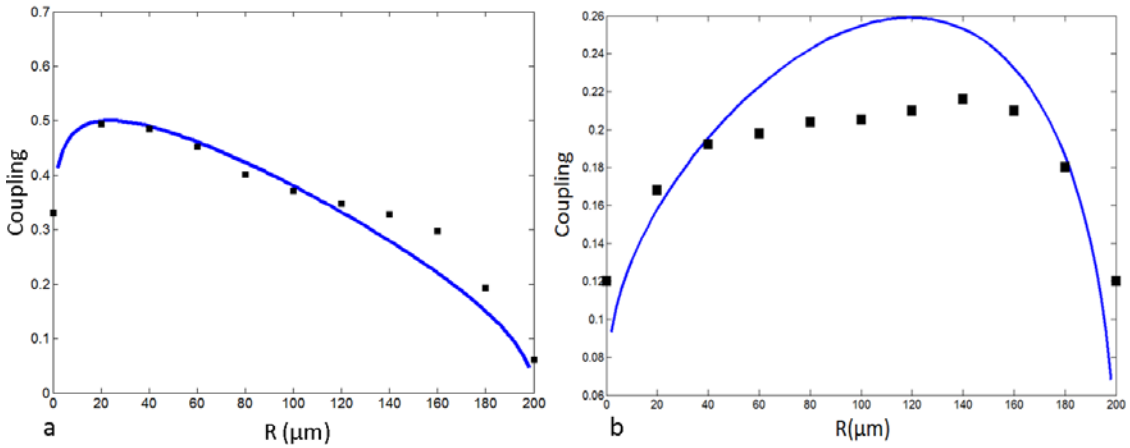

Figure 2.11 Coupling obtained from the theory (solid line), and from full-wave simulations using FEM (dark squares), for a two-wire waveguide with D = 400μm at 1THz (a) the parallel-plate excitation for simulations and $w \times d$ = 1mm × 0.4mm for theory, (b) the dipole excitation for simulations and $w \times d$ = 1mm × 1mm for theory.

Figure 2.11 compares the coupling obtained from the theory with the one from the simulations. In the theoretical calculations, we choose $w \times d$ = 1mm × 0.5mm (equal to the parallel-plate dimensions) for the parallel-plate case, and $w \times d$ = 1mm × 1mm (equal to the cross section of the box) for the dipole one. At the lower limit, when the radii of the wires go to zero, there is no waveguide to support the TEM mode; thus, the coupling should go to zero. Coupling should also go to zero at the higher limit, when the radii of the wires become equal to $D/2$ (the center-to-center distance of the wires, D, is constant and equal to 400μm) because the edges of the two wires touch each other and the waveguide cannot support the TEM mode. Therefore, there should be an optimum value

for the radius corresponding to the peak value of the coupling between the limits. Figure 2.11 shows that the results are consistent with this expectation. The results from the theory and the simulations with the parallel-plate waveguide, depicted in Fig. 2.11(a), show good agreement. Figure 2.11(b) also illustrates the results from the theory and the simulations with the dipole source. They show the same overall behavior even though there are some discrepancies due to neglecting the excitation of radiating and higher-order modes at the input port in the theoretical calculations.

We also studied the case where a plane wave with the cross section of $w \times d$ = 1mm × 1mm impinges a two-wire waveguide with constant radii of the wires, 500 μm, for different center-to-center distances. Figure 2.12 shows the coupling efficiency for this case. D starts from its minimum value, $2R$, where the two wires touch each other and the coupling is zero. As D increases, the waveguide starts to support the TEM mode that overlaps with the field of the plane wave, enhancing the coupling. But when the edges of the wires are too close, the TEM mode supported by the waveguide is mostly concentrated in a very small area between the wires, resulting in small coupling. However, as D becomes larger the field is more distributed on the surface of the wires [23], increasing the overlap area and, in turn, the coupling. This trend continues up to the point that the edge-to-edge distance of the wires is equal to the size of the plane wave.

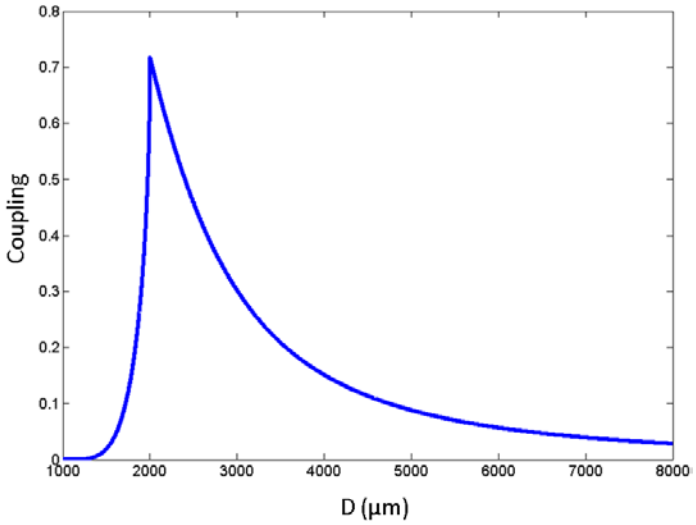

Figure 2.12 Coupling vs. D, for R = 500μm and $w \times d$ = 1mm × 1mm.

This is the point where the TEM mode can capture the most power from the impinging plane wave, as shown in Figure 2.13(a). After that point, the field area with high

amplitude escapes from the plane wave region as shown in Figure 2.13(b), leaving small field overlap and coupling. These results are consistent with the experimental and theoretical results reported in [23], [24].

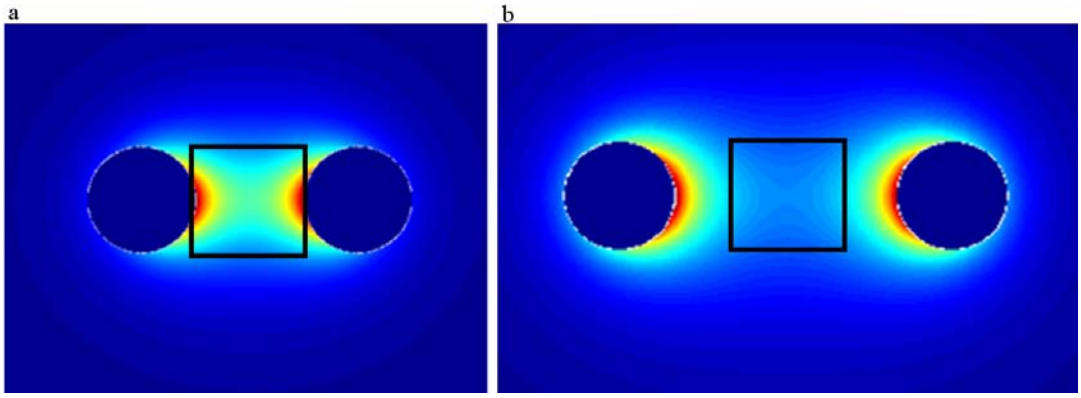

Figure 2.13 (a) overlap region of the plane wave (black square) and the waveguide field for R = 500μm and D = 2mm, (b)overlap when R = 500μm and D = 3mm.

The coupling efficiency is highly dependent on the dimensions of the aperture defining the plane wave impinging the waveguide, as well. If this is large or small compared to the waveguide, the waveguide cannot possibly pick up sizeable power, as clearly shown in Figure 2.13(b). Given the size of the aperture, Eq. 2.48 and Eq. 2.49 can give optimum values for the dimensions of the two-wire waveguide, R and D. But, roughly speaking, the optimum point always corresponds to when the size of the aperture is close to the edge-to-edge distance of the wires, like the case shown in Figure 2.13(a). Note that the proposed method is only accurate when a single TEM mode dominates the behavior of the waveguide. Avoiding higher-order modes limits the dimensions of the waveguide. However, the fact that the linearly-polarized incident field is well-matched with the TEM mode supported by the waveguide alleviates that concern to some extent.

Chapter 3

Slot-lines for Terahertz Waves

Transmission lines are an important part of RF and microwave systems. Generations of high-speed communication systems exploited planar transmission lines like microstrips, striplines, slot-lines, and coplanar striplines to carry electromagnetic waves. Unlike the two-wire waveguide studied in Chapter 2, they are compact, low in cost, and capable of being integrated easily with other components of systems. In the terahertz range, however, loss and dispersion prove to be two major obstacles, limiting the applicability of conventional planar transmission lines.

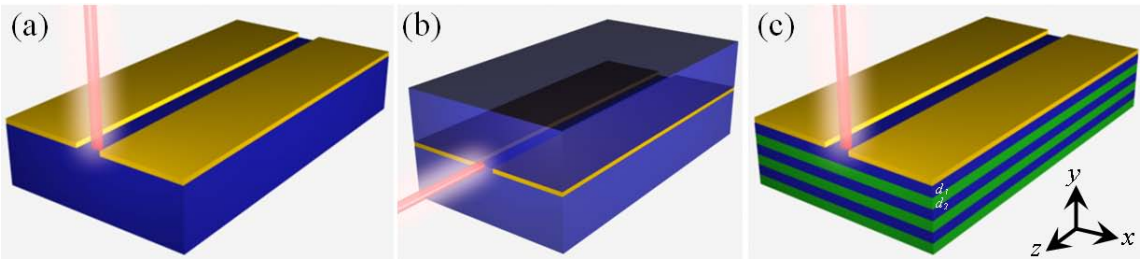

Figure 3.1 (a) Conventional slot-line, (b) slot-line in a homogeneous medium , and (c) slot-line on a layered substrate.

Of many planar alternatives, the slot-line structure with a thin slot in a conductive coating on one side of a dielectric substrate (Fig. 3.1a) is quite compatible with terahertz photoconductive switches. The electrostatic field resulting from the applied bias voltage in the emitter is exactly the same as the field distribution of the propagating mode. This allows essentially perfect coupling efficiency of waves into the transmission lines [44]. However, at higher frequencies where the substrate thickness is larger than the wavelength, the slot-line, like other asymmetrical transmission lines, becomes extremely lossy due to electromagnetic shock-wave radiation [45,46]. This radiation occurs when charges move faster than the phase velocity of electromagnetic radiation in a material [47]. The geometry of conventional slot-lines results in some of the field lines in the dielectric region, with the rest in the air region above the substrate. Hence, in asymmetrical transmission lines, the group velocity of the propagating mode is higher

than the phase velocity in the dielectric, yielding emission of electromagnetic shock-wave radiation (leaky waves) [48,49]. Also, as a result of the phase mismatch at the dielectric-air interface, the slot-line cannot support a pure TEM mode. Therefore, the basic electrical parameters of the slot-line, like the characteristic impedance and the phase velocity vary with frequency, making the slot-line a dispersive line.

In this chapter, we present two solutions to the challenge of shock-wave radiation loss for slot-lines: using a slot-line in a homogeneous medium (Fig. 3.1b), and using a slot-line on a layered substrate (Fig. 3.1c). The former is suitable for broadband applications for it supports a pure TEM mode that is free from cutoff frequency and group velocity dispersion. The latter, on the other hand, is more appropriate for narrowband applications. Theoretical and numerical analyses are used to verify that the slot-line in a homogeneous medium and a slot-line on a layered substrate can be used for guiding terahertz waves with 2 cm^{-1} and 3 cm^{-1} absorption, respectively, due to conductor loss.

3.1 Slot-lines in a homogeneous medium

3.1.1 Theoretical analysis of the slot-line in a homogeneous medium

Analysis of the TEM mode supported by a slot-line in a homogenous medium entails solving the 2D Laplace equation for the electric potential function on the cross-section of the slot-line with fixed potential values on the two metal plates. Conformal mapping can be exploited to solve the problem. The following complex analytic function maps the cross section of the slot-line to two parallel lines like the cross section of a parallel-plate waveguide as shown in Figure 3.2(b,c) [27]:

$$f(z) = \sin^{-1}\left(\frac{z}{s/2}\right). \tag{3.1}$$

The potential function in the region between the two parallel-plate is

$$V = \frac{2V_0}{\pi}\Re e\{f(z)\} = \frac{2V_0}{\pi}\Re e\left\{\sin^{-1}\left(\frac{x+iy}{s/2}\right)\right\}, \tag{3.2}$$

where V_0 is the absolute value of the potential on the plates and s is the separation. The equipotential curves in the uv-plane are simply the lines parallel to the v-axis corresponding to a family of confocal hyperbolas whose foci are located at distance $s/2$ from the origin in the xy-plane:

$$\left(\frac{x}{s/2\cdot\sin\left(\frac{\pi}{2}\cdot\frac{V}{V_0}\right)}\right)^2-\left(\frac{y}{s/2\cdot\cos\left(\frac{\pi}{2}\cdot\frac{V}{V_0}\right)}\right)^2=1\,. \tag{3.3}$$

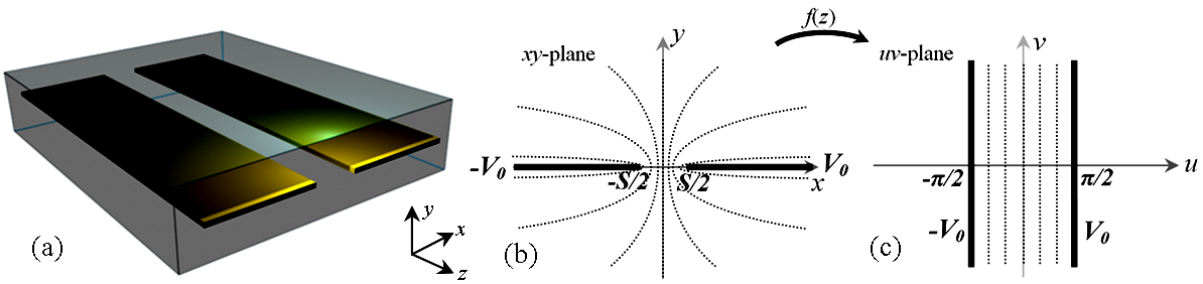

Figure 3.2 (a) Slot-Line in a homogeneous medium, (b,c) mapping the cross section of the slot-line (b) to the cross section of a parallel-plate waveguide, (c) dotted-lines show the constant potential curves.

The asymptotes of these hyperbolas make the angle $(1\text{-}V/V_0)\pi/2$ with the x-axis. The electric field can be derived from the gradient of the potential:

$$\vec{E}=-\nabla V\,, \tag{3.4}$$

that, with some algebraic simplifications, yields

$$\vec{E}=\frac{V_0}{s/2\left(\cos^2(u)+\sinh^2(v)\right)}\left(\cos(u)\cosh(v)\hat{x}-\sin(u)\sinh(v)\hat{y}\right), \tag{3.5}$$

$$\vec{H}=\frac{1}{\eta}\hat{z}\times\vec{E}\,, \tag{3.6}$$

where,

$$\begin{cases}u=\Re e\left\{\sin^{-1}\left(\dfrac{x+iy}{s/2}\right)\right\}\\ v=\Im m\left\{\sin^{-1}\left(\dfrac{x+iy}{s/2}\right)\right\}\end{cases}, \tag{3.7}$$

and η is the intrinsic impedance of the surrounding medium. Note that the metal plate thicknesses are assumed to be zero here. The effect of the finite thicknesses of the plates will be discussed later.

Figure 3.3(a) shows the equipotential curves and the electric field for a slot-line with 10 μm separation. Around the gap between the plates, the potential function varies significantly with a small spatial change, resulting in a high field amplitude, especially at the edges. Far from the gap, on the other hand, the potential function has a slow spatial

change, leading to a small field amplitude as shown in Figure 3.3(b). These results are consistent with the ones from numerical simulations using the finite-difference frequency domain (FDFD) method reported in [50].

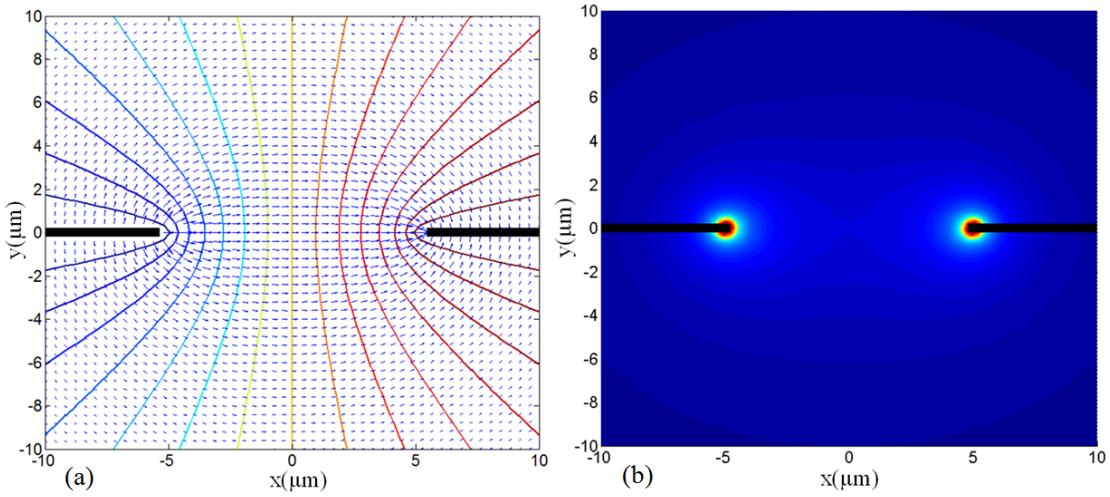

Figure 3.3 (a) Equipotential curves and electric field vector (blue arrows), (b) electric field amplitude square.

3.1.2 Loss estimation of the slot-line in a homogeneous medium

The time-averaged power absorbed per unit area due to ohmic losses in the body of the conductor can be determined by Eq. 2.15. Eqs. 3.5 and 3.6 give the tangential magnetic field at the surface of the conductors with infinitesimal thicknesses. For small, but not zero thicknesses of the conductors, a good estimate can be obtained by approximating the planar metal plates with two branches of a hyperbola whose asymptotes make very small angles with the *x*-axis, like the ones shown in Figure 3.4. This hyperbola corresponds to the lines $u = \pm u_0$ in the *uv*-plane when u_0 is very close to $\pi/2$ and depends on the thickness of the plates.

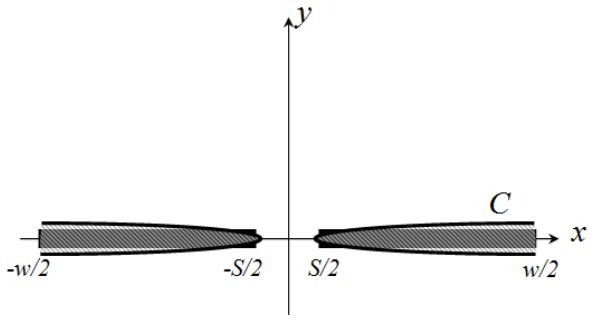

Figure 3.4 Approximation of two thin planar plates by two branches of a hyperbola.

The power loss per unit length of the transmission line is then [29]

$$\frac{P_{loss}}{L} = \frac{\mu_c \omega \delta}{4} \int_C {H_{\parallel}}^2 dl = \frac{\mu_c \omega \delta}{4} \int_C \frac{{E_{\perp}}^2}{\eta^2} dl \,, \tag{3.8}$$

where *C*, the domain of integration, is the hyperbola shown in Figure 3.4. The following parameterization of the curve *C* is used to calculate the integral:

$$\begin{cases} x = \frac{s}{2} \sin(u_0) \cosh(v) \\ y = \frac{s}{2} \cos(u_0) \sinh(v) \end{cases}, \tag{3.9}$$

that yields,

$$\frac{P_{loss}}{L} = \frac{\mu_c \omega \delta}{4} \left[4 \frac{{V_0}^2}{\eta^2} \left(\frac{2}{s} \right) \int_0^{v_0} \frac{dv}{\sqrt{\cos^2(u_0) + \sinh^2(v)}} \right], \tag{3.10}$$

where,

$$v_0 = \cosh^{-1}(w/s). \tag{3.11}$$

The plate width is assumed to be much larger than the separation ($s << w$). Otherwise the equipotential curves on the *uv*-plane in Figure 3.2(c) cannot be simply the lines parallel to the *v*-axis. The power flowing on the lossless line, is

$$P_0 = \frac{1}{2} \Re e \left\{ \int_{S'} \left(\vec{E} \times \vec{H}^* \right) . \vec{ds} \right\}, \tag{3.12}$$

where *S'*, the surface of integration, is the cross section of the transmission line. Calculation of P_0 includes a complicated surface integral on the cross section of the slot-line. However, the integration can be calculated in the simpler *uv*-plane shown in Figure 3.2(c) instead that yields

$$P_0 = \frac{{V_0}^2}{2\eta} (2u_0)(2v_0). \tag{3.13}$$

The attenuation constant is then

$$\alpha_c = \frac{P_{loss}/L}{2P_0} = \frac{\mu_c \omega \delta}{\eta} \left[\frac{1}{2 s u_0 v_0} \int_0^{v_0} \frac{dv}{\sqrt{\cos^2(u_0) + \sinh^2(v)}} \right], \tag{3.14}$$

where v_0 depends on *s* and *w* by Eq. 3.12, and u_0 depends on the thickness of the metal plates. Eq. 3.14 shows how conductor loss changes with the waveguide dimensions, the

operating frequency, and the waveguide materials including materials of the metal plates and surrounding medium (through skin depth of the metal and intrinsic impedance of the medium). The total loss also includes dielectric loss that depends on the material of the surrounding medium. Using crystalline silicon, crystalline GaAs, and crystalline germanium as propagation media, all of which have very low loss tangent in the THz frequency range [51], minimizes the dielectric loss. In Section 3.3, we discuss how conductor loss changes with slot width and metal plate thickness and we estimate the dielectric loss for the slot-line in GaAs.

3.2 Slot-lines on a layered substrate

The previous section discusses slot-lines in a homogenous medium. But a slot-line on one side of a dielectric substrate is a more suitable structure if surface mounted components are required to be integrated with the waveguide. Also, optical excitation of such THz slot-lines on one side of a substrate are easier compared to the slot-lines in a homogeneous medium. However, large loss due to electromagnetic shock-wave radiation [45] renders these planar waveguides useless for THz frequencies. In this section, we present a novel slot-line structure on one side of the substrate that is free from radiation loss.

A slot-line on a layered substrate, shown in Figure 3.1(c), can also solve the problem of shock-wave radiation. The slot-line on a layered substrate has a continuous translational symmetry in the *z*-direction leading to the modes with the form e^{ikz} as an eigenfunction [52]. Therefore, the modes must have the form

$$E_k(x,y,z) = E_0(x,y)e^{ik_z \cdot z}, \tag{3.15}$$

where the wave number k_z is a conserved quantity due to the continuous translational symmetry. In the lower half-space, the periodic substrate also creates a discrete translational symmetry in the *y*-direction, resulting in the modes in Bloch state forms:

$$E_k(x,y,z) = u_{k_y}(x,y)e^{ik_y y}e^{ik_z z}, \tag{3.16}$$

where u_{ky} is a periodic function of *y* with the same periodicity as the substrate. This periodicity induces a so-called "photonic band gap" in the band structure of the crystal. A mode that has a frequency within the gap cannot propagate through the crystal and has an

amplitude that decays exponentially into the crystal since k_y becomes an imaginary number. The size of the band gap depends on the thickness of the layers, periodicity, dielectric constants of the layers, and frequency. For two materials with refractive indices n_1 and n_2 and thicknesses d_1 and $d_2 = a - d_1$ the normal-incidence gap is maximized when $d_1 n_1 = d_2 n_2$ (a is the periodicity) [53]. The frequency at the middle of the gap ω_m in this case is [54,55]

$$\omega_m = \frac{n_1 + n_2}{4 n_1 n_2} \cdot \frac{2\pi c}{a}, \tag{3.17}$$

with the corresponding vacuum wavelength λ_m that satisfies the quarter-wavelength conditions: $\lambda_m / n_1 = 4d_1$ and $\lambda_m / n_2 = 4d_2$.

The air-substrate interface breaks the translational symmetry, making the structure sustain localized modes within the photonic band gap. These are evanescent modes on both sides of the surface with their field spatially bounded in the direction perpendicular to the substrate as shown in Figure 3.5(a). The metal plates of the slot-line also confine the waves in the x-direction (Figure 3.1c), leaving only the z-direction for waves to propagate. The field distribution of the surface mode supported by the slot-line on a layered substrate is difficult to obtain analytically due to the presence of two metal plates of the slot-line. However, we present the mode profile supported by the waveguide obtained from the numerical simulations using the Finite Element Method (FEM). Figure 3.5(b) shows the electric field distribution of the surface mode supported by a slot-line on a quarter-wave stack of Si/SiO_2 with 10 μm separation of the metal plates. The field amplitude is exponentially damped on both sides of the substrate, as expected from the theory. Similar to the slot-line in a homogeneous medium, the field is highly concentrated at the edges of the plate, but more distributed inside the substrate due to higher average refractive index of the substrate.

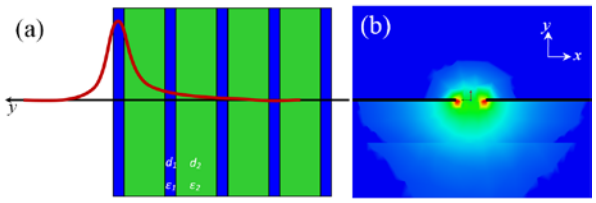

Figure 3.5 (a) Electric field amplitude associated with a localized mode at the surface of a layered substrate, (b) the electric field distribution for a slot-line on a periodic Si/SiO_2 layered substrate (d_1 = 13.8 μm, d_2 = 37.5 μm, s = 10 μm, w = 500 μm) from a 3D full-wave FEM simulations.

3.3 Results and discussion

Figure 3.6 shows simulation results for slot-lines obtained from full-wave 3D FEM simulations using the Ansoft HFSS frequency-domain solver. Three cases are considered: a conventional slot-line on a GaAs substrate, a slot-line in GaAs, and a slot-line on a periodic Si/SiO_2 layered substrate. The slot-lines are excited by a surface current source at 1THz, emulating a current generated in a terahertz photomixer. The simulations are bounded by a rectangular box with 0.5 mm × 0.5 mm × 2 mm size, and with radiation boundaries assigned to the walls to avoid reflection, as shown in Figure 3.6. The absorption coefficient can be calculated from the power measured at two different lengths of the transmission line.

For the slot-line on the half-space GaAs, the substrate/superstrate mismatch causes large radiation loss into the substrate as clearly shown in Figure 3.6(a). This radiation loss changes in proportion to the third power of frequency. Simulation results show 23.9 cm^{-1} loss for a slot-line on a half-space GaAs substrate with 20 μm separation of the plates. However, conductor loss that changes in proportion to the square root of frequency is the only dominant absorption mechanism for the slot-line in GaAs, allowing significantly longer distance wave propagation (Figure 3.6b).

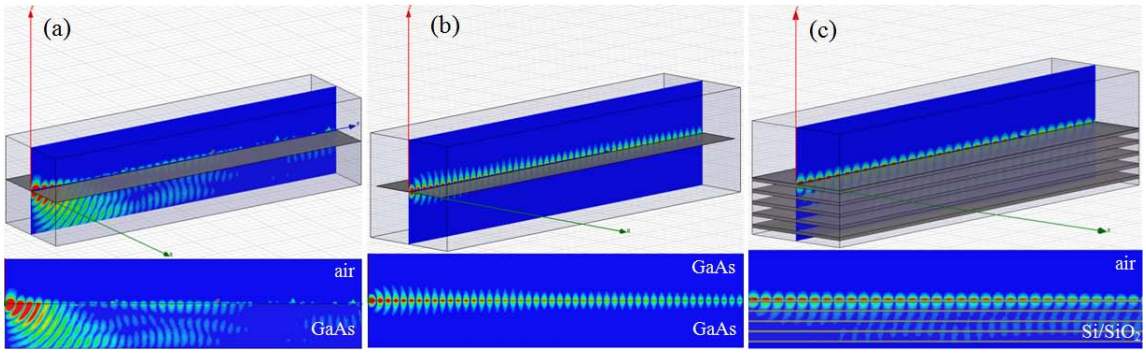

Figure 3.6 The electric field amplitude from a 3D full-wave simulations with FEM using Ansoft HFSS for (a) a slot-line on a half-space GaAs substrate, (b) a slot-line in GaAs, and (c) slot-line on a periodic Si/SiO_2 layered substrate (d_1 = 13.8 μm, d_2 = 37.5 μm), all with s = 20 μm, *w* = 500 μm.

Figure 3.7(a) shows the conductor loss versus *s*, the slot width, obtained both from the theory (Eq. 3.14) and the simulations at 1 THz for a slot-line in GaAs. At the lower limit, when the separation goes to zero, the edges of the two plates touch each other and the transmission line cannot support the TEM mode. The conductor loss is a decreasing

function of s. There is also a knee in the curve after which the loss changes rather slowly. The results from the simulations, illustrated by green squares in Figure 3.7a, show good agreement with the theoretical expectations (blue solid line). The conductor loss for slot-lines with enough separation (> 5 μm) is in the order of 2 cm^{-1}, consistent with the conductor loss experimentally measured on a 20-mm-long coplanar transmission line with 15 μm separation of the lines at 1THz in [45]. In that paper, the relationship $\alpha = A_c f^{1/2} + A_{rad} f^3$ was presented for the absorption, where A_c and A_{rad} are resistive and radiative loss coefficients, respectively, and f is the frequency in THz. Curve fitting of experimental data resulted in $A_c = 2$ cm^{-1}, $A_{rad} = 6.5$ cm^{-1}.

Figure 3.7(b) shows the conductor loss versus u_0 for a slot-line with $s = 10$ μm, $w = 500$ μm made out of gold in GaAs. At $u_0 = \pi/2$ the plate thickness is zero, making infinitely high conductor loss. For the finite thickness, however, the loss is relatively independent of the thickness, as expected since the current density is confined to such a small thickness (skin depth δ = 78.6 nm for gold at 1THz) just below the surface of the conductor.

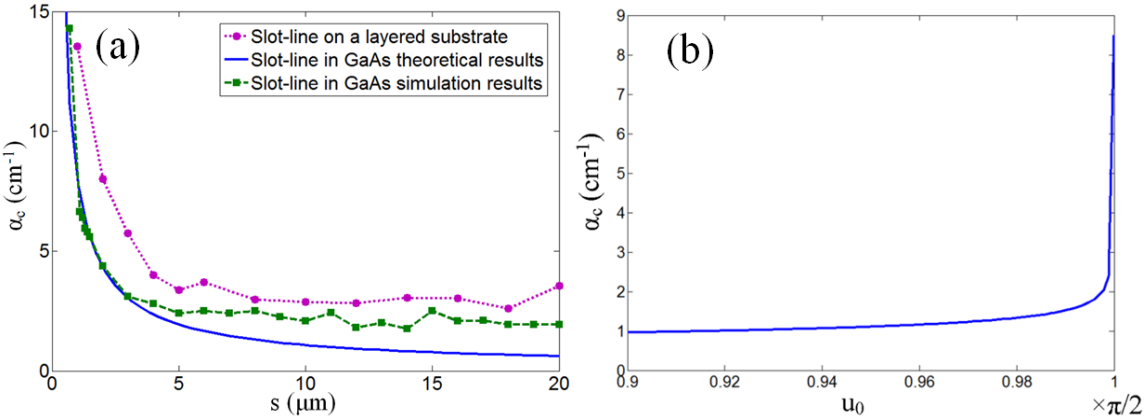

Figure 3.7 (a) The conductor loss vs. separation s, for slot-line made out of gold in GaAs, obtained from the theory (solid blue line) and from the simulations (dashed-line with green squares), and for a slot-line on a quarter-wave stack of Si/SiO_2, obtained from the simulations (dotted-line with purple circles), (b) the conductor loss for slot-line in GaAs vs. u_0, for $s = 10$μm.

For the waveguide that is completely filled with a homogenous dielectric, the dielectric loss can be calculated from the propagation constant regardless of the type of guide [56]. For instance, the dielectric loss for crystalline high-resistivity GaAs is measured to be 0.5 cm^{-1} at 1THz [51]. The total loss is the sum of dielectric and conductor loss. For a slot-line with more than 10 μm separation and more than 100 nm thickness of the plates, the

total loss would be about 2.5 cm^{-1}, an order of magnitude lower than the slot-line on a dielectric substrate (23.9 cm^{-1}) at 1THz. This shows that the radiation loss is the dominant loss for the asymmetric slot-line, consistent with the experimental results in [45,46,57].

For the slot-line on multilayer substrate, shown in Figure 3.6(c), a quarter-wave stack of Si/SiO_2 ($4d_1 = \lambda / n_1$, $4d_2 = \lambda / n_2$) is chosen to maximize the photonic band gap size [52,53]. Figure 3.6(c) shows that the multilayer film can effectively prevent wave radiation into the substrate, making this slot-line efficient for guiding terahertz waves. Figure 3.7(a) (purple circles) shows the conductor loss versus *s*, the separation of the plates, obtained from numerical simulations at 1THz. Similar to the slot-line in a homogeneous medium, the conductor loss is a decreasing function of *s*. The results show the conductor loss for this slot-line with enough separation (> 5 μm) is in the order of 3 cm^{-1}.

Chapter 4

Experimental Results

After developing the theory of the two-wire and slot-line waveguides, we conducted series of experiments to verify the performance of the waveguides. This chapter deals with the details of the experiments and results. First, a THz generator and a detector are needed to test the waveguide. We use Photoconductive Antennas (PCAs) as the transmitter and the receiver. The PCA is basically a small dipole antenna deposited on an ultra-fast semiconductor substrate like Low Temperature-Grown GaAs (LTG-GaAs) as shown in Figure 4.1. A comprehensive description of LTG-GaAs can be found in [58]. The optical pulse excites electron-hole pairs in the gap area inside the semiconductor. The excited carrier density increases with a rise time roughly equal to the optical pulse rise time (about 30 fs). The photo-carriers then recombine in the average time equal to the carrier life time of the substrate, decreasing carrier density with a fall time equal to the carrier life time. Using a fast substrate like LTG-GaAs with less than 1 ps carrier lifetime, we can have the carrier density pulse in the ps range or THz bandwidth.

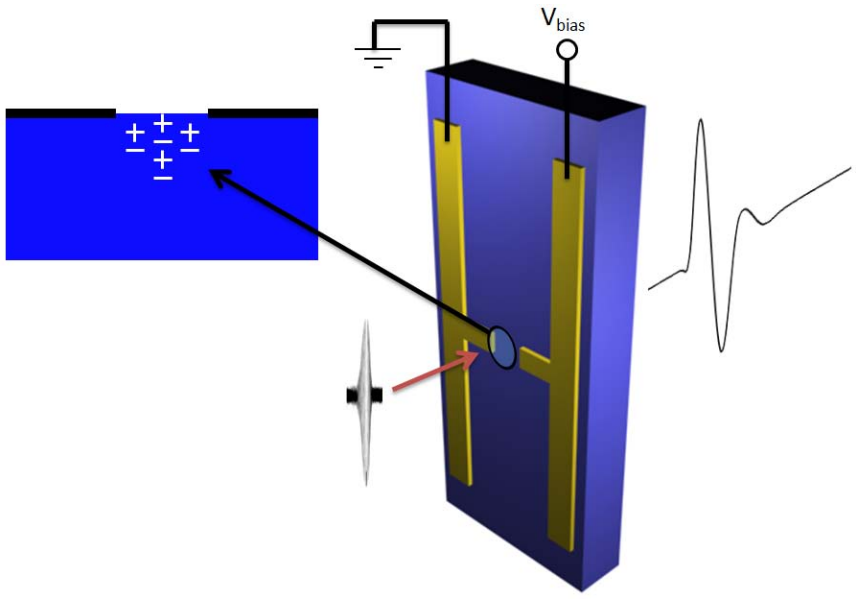

Figure. 4.1 THz generation by photoconductive antenna (PCA).

This pulsed free carrier density produces a ps-pulsed modulated conductivity across the gap. The bias voltage creates an electric field across the gap, accelerating the photo-carriers. The acceleration of charges, in turn, creates electromagnetic pulse radiation in the ps range.

As an optical source, we use a Ti-Sapphire laser from KMLAbs (Kapteyn-Murnane Laboratories) shown in Figure 4.2, capable of generating less than 25 fs optical pulses at 810 nm with 80 MHz pulse repetition rate and more than 150 mW average power.

Figure 4.2 KMLabs fs Ti-Sapphire Laser.

Figure 4.3 shows a typical broadband THz pulse setup. A 30 fs optical pulse from a Ti-Sapphire laser is divided into two beams by a 50/50 beam splitter, one for the transmitter branch and the other for the receiver branch. In the transmitter branch, the beam passes through a delay line and then is focused on the transmitter PCA. The biased transmitter generates ps pulses that can be detected by the receiver. The delay line comprises of a retro-reflector mounted on an automatic translational stage connected to a computer.

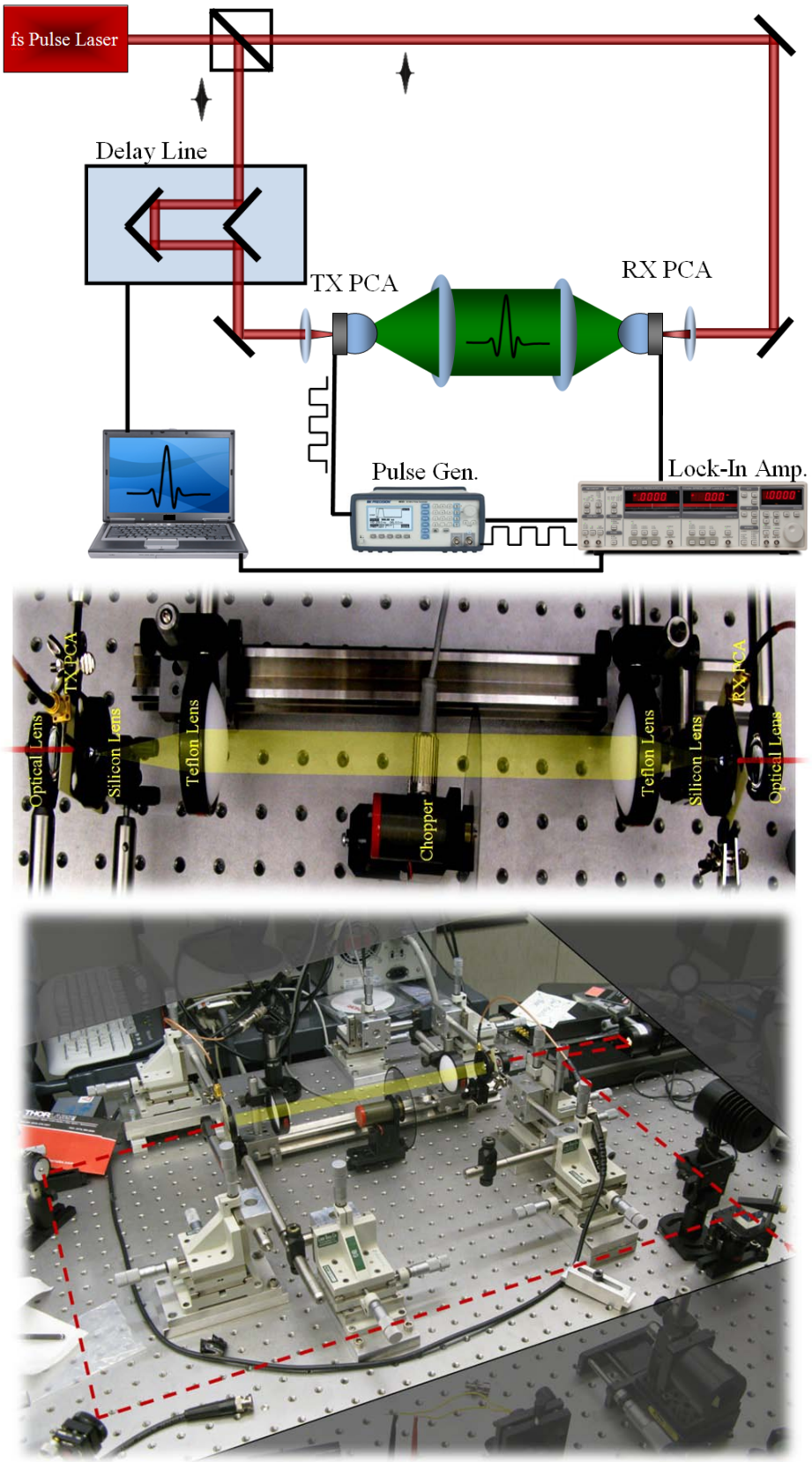

Figure 4.3 Broadband THz pulse setup.

The receiver optical pulse excites electron-hole pairs in the antenna gap of the receiver PCA, resulting in an ultra-fast pulsed carrier density in the ps range. The conductivity of the antenna gap changes in proportion to the pulsed carrier density. A THz pulse impinging on the receiver antenna induces a pulsed voltage across the gap. The electric field amplitude of this THz pulse can be probed by measuring the low-frequency or down-converted component of receiver current ($I(t) = G(t) \times V(t)$). A highly sensitive Lock-In amplifier is used to measure this receiver current. Maximum current is measured when the induced voltage peak coincides the carrier density peak, and no current is measured when there are no excited carriers or zero induced voltage. Therefore, sweeping the delay line stage, which changes the time at which the THz pulse reaches the receiver, convolves the induce pulsed voltage with the pulsed conductivity, resulting in the pulse waveform in the time-domain. Taking the Fourier transform of this waveform will give the spectrum of the received THz pulse. The bias voltage of the transmitter is chopped at 100 Hz so that the Lock-In amplifier at the receiver can lock to that frequency and filter out other frequencies, decreasing noise level at the receiver. Two silicon lenses and two Teflon lenses are used to focus the THz beam generated by the transmitter onto the receiver.

One main challenge with the setup shown in Figure 4.3 is the alignment. The transmitter and receiver have to be aligned with both optical pulses and THz waves, making it difficult and yet critical to align the system. Another downside of this setup is that THz optics components are usually bulky, making the spectrometer rather large. Also, THz waves cannot be focused very well on the sample. The diffraction limit theoretically restricts the best focus to the half of the wavelength (150 μm at 1 THz).

A waveguide structure overcomes these difficulties. A THz setup with a waveguide is less sensitive to alignment, so a good THz waveguide can help the integration of the THz setup. Also, THz waves can be confined in sub-wavelength dimensions using two-wire and slot-line THz waveguides.

4.1 Experimental setup and results for the two-wire waveguides

To make a two-wire waveguide we need two straight cylindrical metal wires supported by a holder that has low loss at THz frequencies. Gold is obviously the best choice for the material of wires in terms of conductivity. But gold is soft, making it difficult to have two

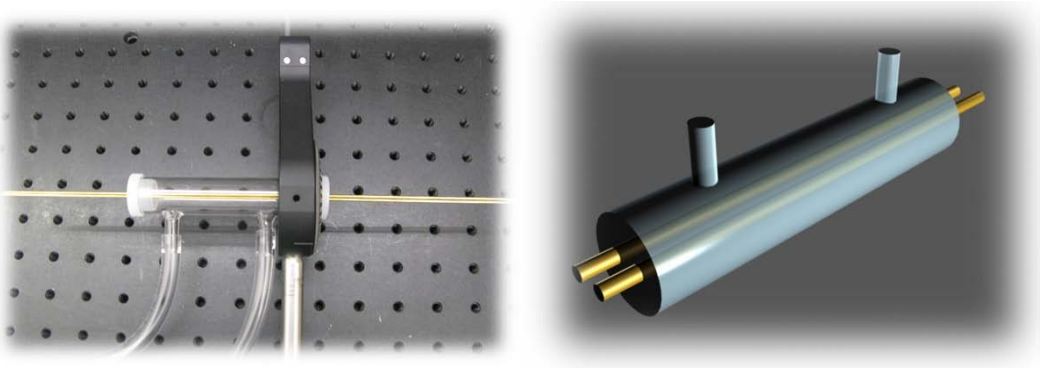

Figure 4.4 12-inch-long brass two-wire waveguide within a glass tube supported by two plastic end caps.

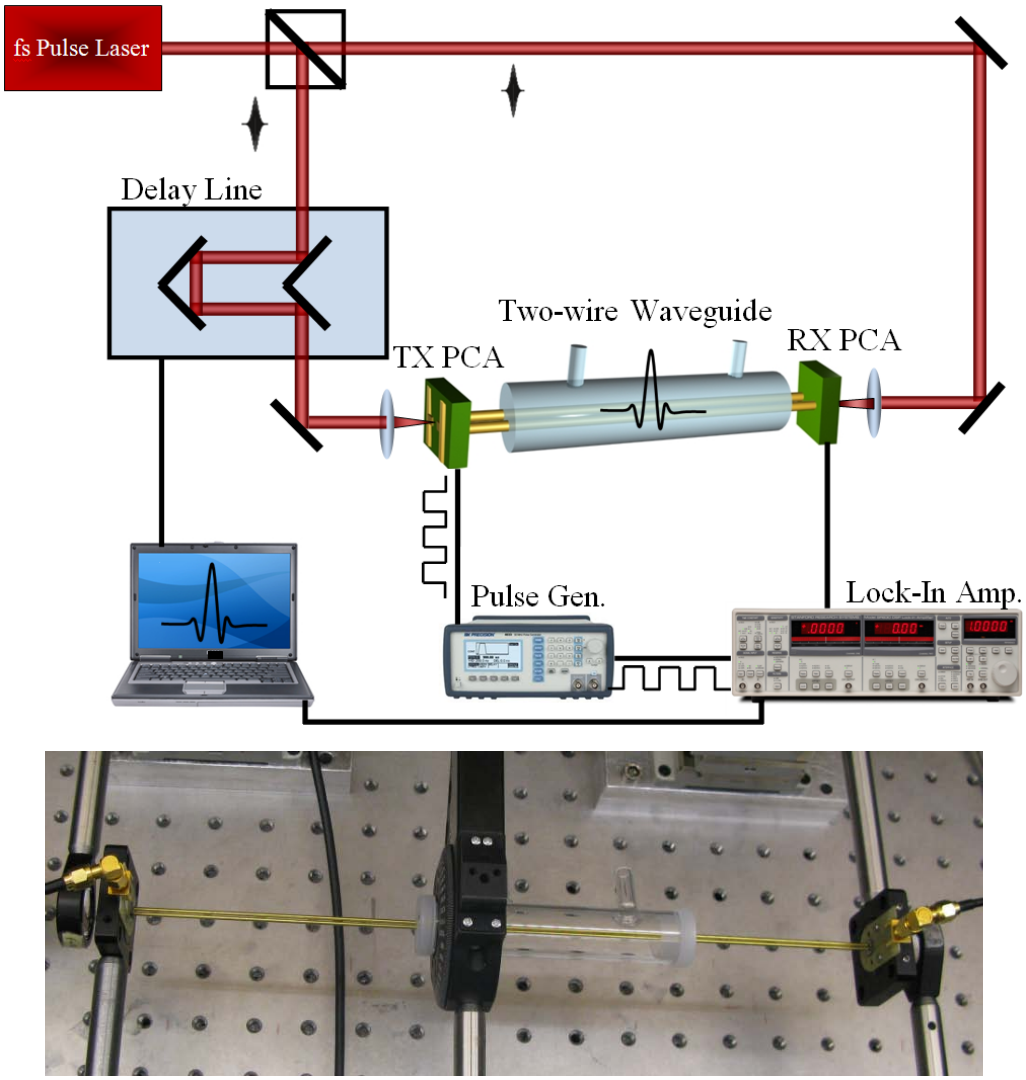

Figure 4.5 Broadband THz setup with a 12 inch, brass two-wire waveguide with 1.6 mm diameter and 2 mm center-to-center distance of the wires.

straight wires along the entire waveguide. So we can either use hard rods with a layer of gold deposited on them or use brass that is hard enough to stand straight and has fairly good conductivity. The two wires are supported within a glass tube between two plastic end caps as shown in Figure 4.4. This structure is particularly designed to be used as a long-interaction-range gas-phase sensor. Gas inlet and outlet ports allow nitrogen purge gas and the admission of gas phase samples.

To test the performance of the waveguide, we replace the THz optics of the setup shown in Figure 4.3 with a 12-inch-long brass two-wire waveguide, with 1.6 mm diameters and 2 mm center-to-center distance of the wires, shown in Figure 4.5. PCAs used as the source and detector are TERA15 THz antenna from MenloSystems. Although these were originally designed to be optically excited at 1550nm, we used 810nm due to the limited frequency range of the fs Ti-Sapphire laser being used.

Figure 4.6 compares the result obtained from the setup with THz optics components (purple solid-line) with those from the setup with the two-wire waveguide (blue dashed-line). A higher signal amplitude is delivered to the receiver by the waveguide, confirming low loss operation of the waveguide. There is also no pulse broadening, indicating dispersion-free propagation of THz waves along the waveguide.

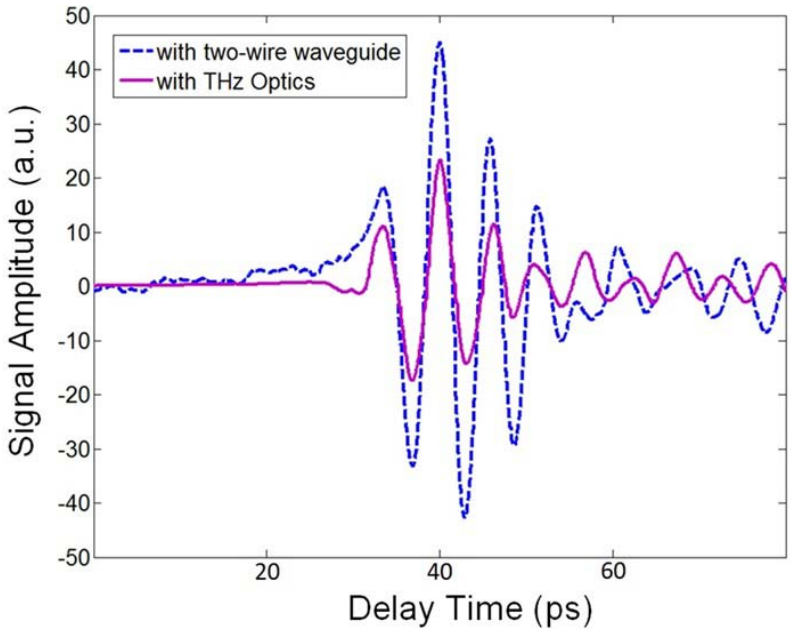

Figure 4.6 Comparison of results obtained from the setup with THz lenses (purple solid line), and from a 12 inch, brass two-wire waveguide with 1.6 mm diameter and 2 mm center-to-center distance of the wires.

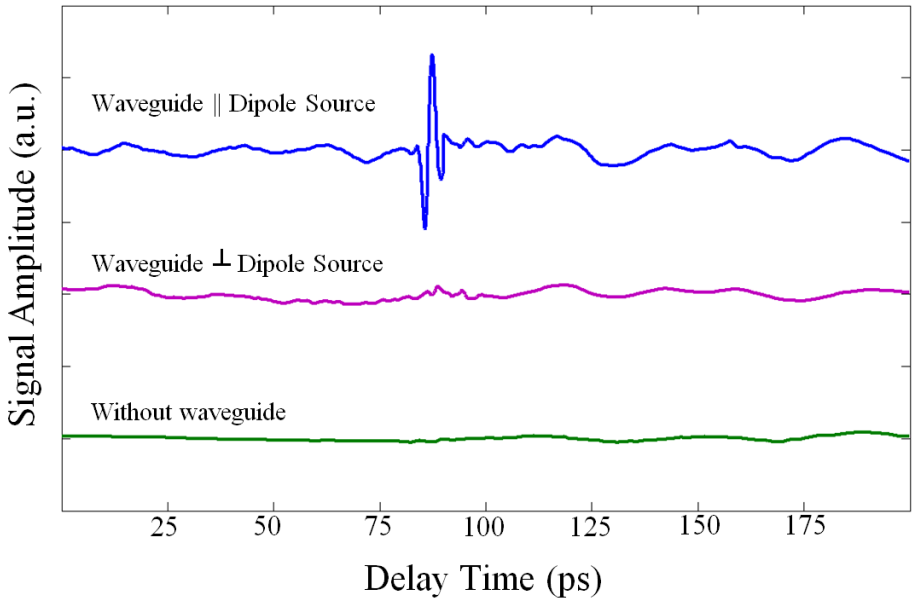

Figure 4.7 Electric field amplitude vs. delay time detected at the receiver for three cases: waveguide parallel to the dipole source (blue line), waveguide perpendicular to the dipole source (purple line), and waveguide removed (green line).

Being designed to operate at 1550 nm, PCAs from MenloSystems excited at 810 nm do not give the best response in terms of the pulse width. Therefore, we replace them with LTG-GaAs PCA-40-05-10-800-a from BATOP Optoelectronics specifically designed to operate at 810 nm. We conducted the THz waveguide experiments for three cases: waveguide parallel to the dipole source, waveguide perpendicular to the dipole source, and waveguide removed. Figure 4.7 compares the results. A ps pulse is detected in the first case where the waveguide is parallel to the dipole source and no signal is detected in the other cases. When the waveguide is perpendicular to the dipole source, the polarization of waves impinging on the input port of the waveguide is completely mismatched with the TEM mode supported by the waveguide, preventing proper excitation of the TEM mode. Due to the high refractive index of the PCA substrate (n = 3.4), outgoing waves from the source are strongly diffracted at the substrate-air interface. Therefore, without the waveguide, the power density at the receiver, 30 cm apart from the transmitter, is too small to be detectable. However, when the waveguide is parallel to the dipole source, the polarization of incident waves is well-matched with the TEM mode of the waveguide, resulting in efficient coupling. Given the low loss of the waveguide,

coupled waves are effectively transferred to the receiver. Figure 4.8 shows the detected THz signal from the two-wire waveguide setup in the time and frequency domains.

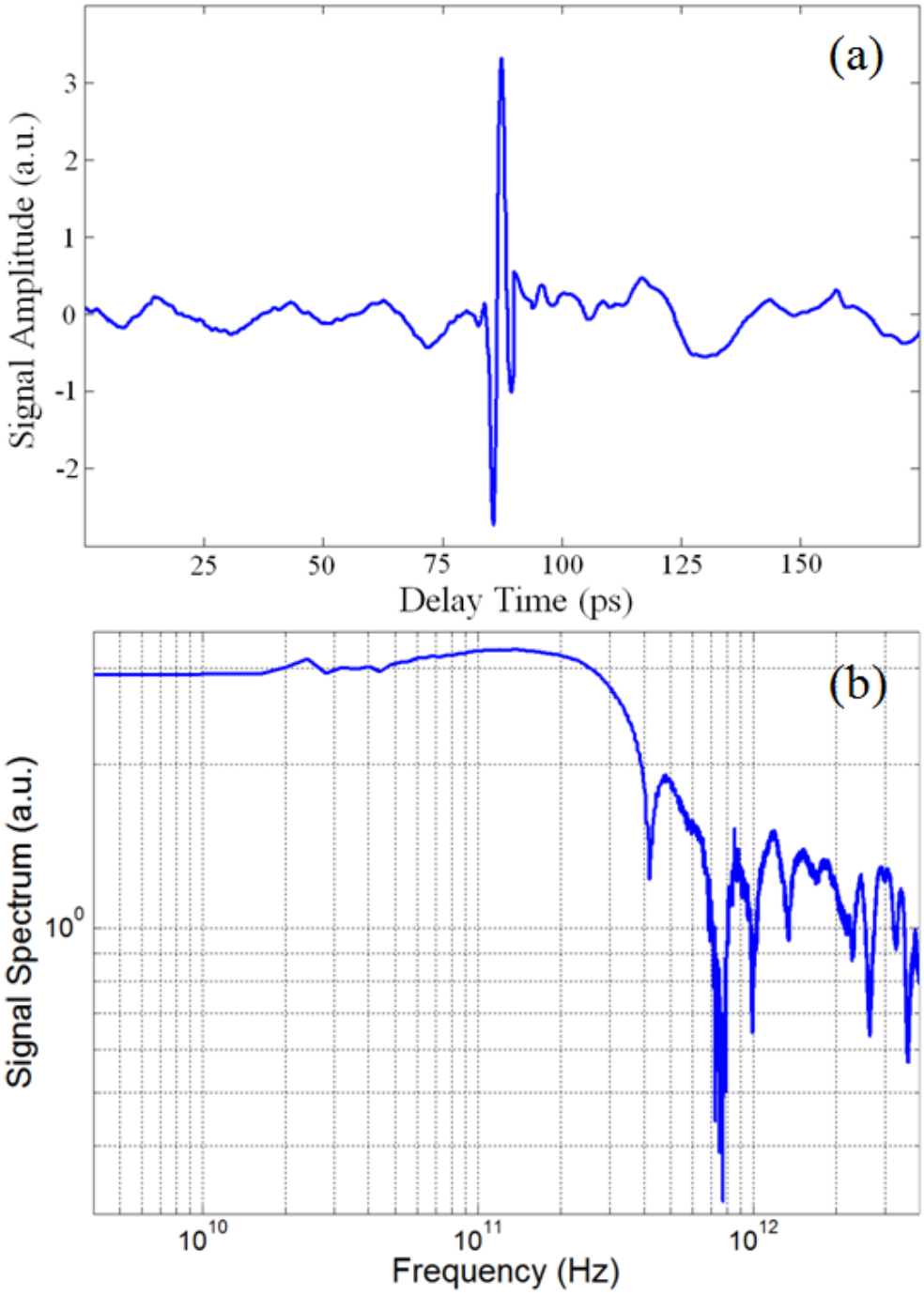

Figure 4.8 The detected signal from the two-wire waveguide setup in (a) time-domain, (b) and frequency-domain.

Figure 4.9 also compares the results of the two-wire waveguide with the results with THz optics components including two silicon lenses and two Teflon lenses. About nine times higher signal amplitude is detected at the receiver for the waveguide setup.

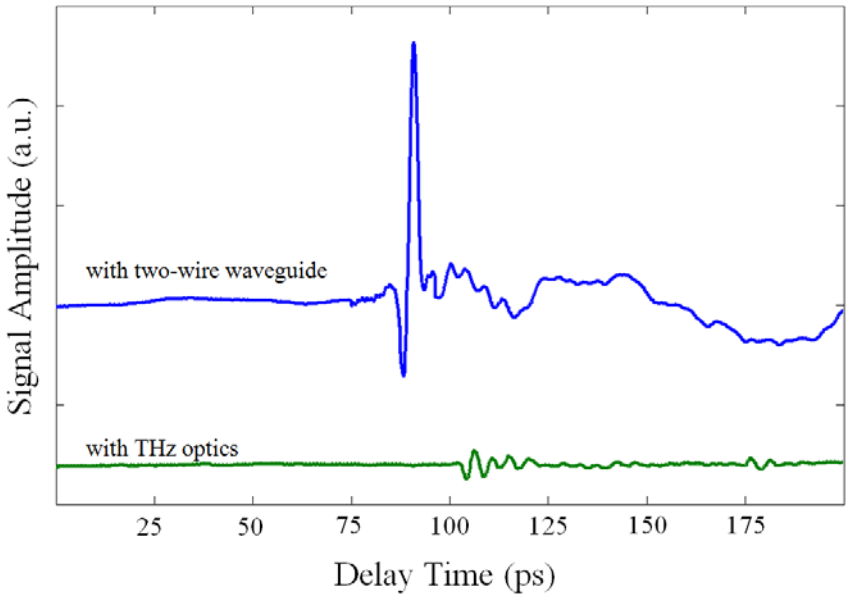

Figure 4.9 Electric field amplitude vs. delay time detected at the receiver for THz setup with the two-wire waveguide (blue line) and THz setup with THz optics components (green line).

4.2 Experimental setup and results for the slot-line in GaAs

We used the THz broadband setup shown in Figure 4.10 to test the slot-line in GaAs. At the generation side, a bias voltage was applied across the plates of the slot-line to accelerate photo-excited carriers. This creates a current pulse that, in turn, excites the propagating mode of the waveguide. The electromagnetic pulse will be detected by another fs optical pulse after propagation along the slot-line to the receiver. Exciting electrons and holes, the second optical pulse creates a ps pulsed carrier density, modulating the conductivity of the antenna gap. When the THz pulse reaches the receiver, the pulsed electric field drives photo-excited carriers, producing a current in the receiver. The current amplitude, measured by a Lock-In amplifier at the receiver, changes in proportion to the electric field and conductivity. Sweeping the delay line stage results in the pulse waveform in the time-domain in the same way as prior setups. The fs optical pulse of the transmitter is chopped at 100 Hz to allow the Lock-In amplifier to filter out other frequencies and reduce the noise level at the receiver.

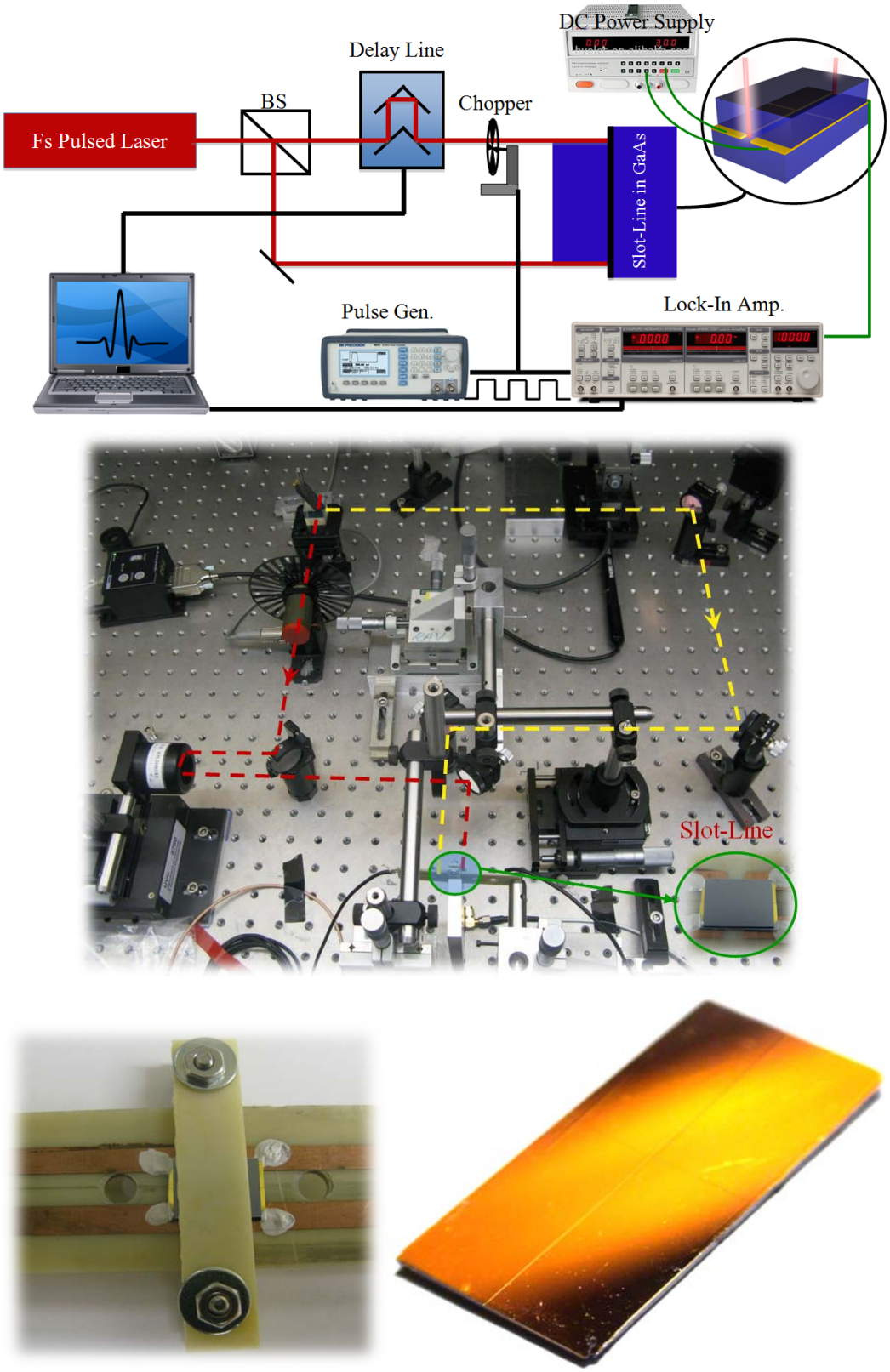

Figure 4.10 THz setup used to test slot-line in GaAs.

There is a small gap in the line to isolate the receiver side from the bias voltage at the generation side. This gap behaves like a coupling capacitor, blocking out very low frequency signals including DC voltage while passing high frequency ones. The small gap (less than 10 μm) does not create significant reflection at THz frequencies, according to the data obtained from FEM simulations using Ansoft HFSS. For the fabrication of the slot-line in GaAs, we used well-known UV-lithography including the following steps:

- depositing 500 μm AZ5214 photo-resist on the GaAs sample by spin coater (5000 rpm for 1 min),
- baking the sample with photo-resist for 1 min at 90 degrees Celsius to harden the photo-resist layer,
- UV exposing for 14 seconds with the mask on the sample,
- removing photo-resist of the exposed area by AZ 300 MIS developer for 1:40 min., rinsing with water, and blow drying the sample,
- depositing 2 nm Cr or Ti and 100 nm gold by E-beam deposition (Cr or Ti acts as an adhesion layer between GaAs and gold),
- and finally removing the gold and Cr in the exposed area by Acetone.

Another GaAs wafer is placed on top of the sample as a superstrate. Two circuit boards and two screws hold the two pieces together with a bit of pressure to make sure there is no significant air gap, relative to the THz wavelength, between them as shown in Figure 4.10.

Figure 4.11 shows the experimental results we obtained from a slot-line with 20 μm gap on a Semi-Insulating GaAs (SI-GaAs) substrate with about 400 ps carrier lifetime. The fs optical pulse of the transmitter increases the carrier density with 30 fs rise time. Photo-excited carriers then recombine in the average time equal to the carrier lifetime of SI-GaAs, reducing the carrier density. The 20V bias voltage across the slot of the generator accelerates excited carriers, creating a current pulse. This current pulse excites the TEM mode of the slot-line in GaAs and this propagates along the waveguide to the receiver according to the theory we developed in Chapter 3. Another fs optical pulse modulates the conductivity of the receiver slot. The convolution of the electric field pulse of the TEM mode with the pulsed conductivity of the receiver is obtained by sweeping the delay line translational stage.

We measured a pulse with high signal-to-noise-ratio with width of about 400 ps, consistent with the carrier lifetime of SI-GaAs. The waveguide loss, calculated from signals measured for two different lengths of the slot-line, was 0.02026 cm^{-1}. The conductor loss calculated by Eq. 3.14 in Chapter 3 for the structure in question is 0.013 cm^{-1}. The loss tangent of SI-GaAs in the GHz range is 5.6×10^{-3} [59], which results in dielectric loss of 2.1×10^{-3} cm^{-1}. Therefore, the expected total loss, 0.0151 cm^{-1}, obtained from the theory developed in Chapter 3 is in good agreement with loss measured experimentally by the setup shown in Figure 4.10.

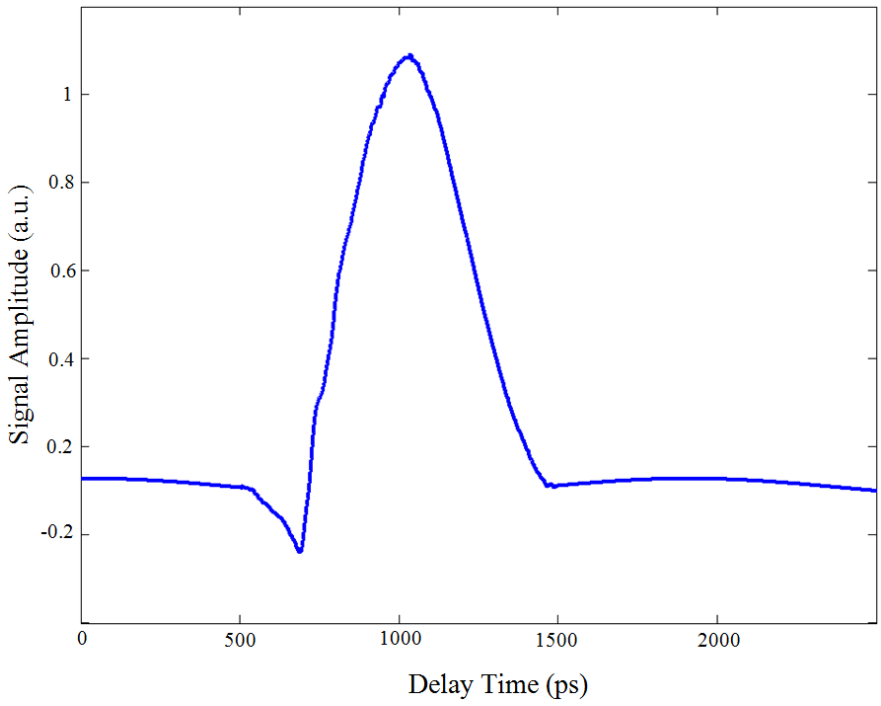

Figure 4.11 Electric field amplitude vs. delay time detected at the receiver for a slot-line with 20 μm gap in SI-GaAs.

Figure 4.12 shows the experimental results we obtained for a 1 cm-long slot-line on a 1.2 μm-thick LTG-GaAs layer grown on a SI-GaAs substrate. This sample was made in the MBE lab at the University of Victoria. Another SI-GaAs wafer is placed on top of the sample to avoid radiation loss. Results from the well-known pump-probe technique on this sample showed 12 ps carrier lifetime. Also, the AFM (Atomic Force Microscopy) image of this sample reveals a high surface roughness due to relaxation of the LTG-GaAs layer on the SI-GaAs substrate that degrades photo-excitation process. We measured 20 μA photo-current with 20V bias voltage for this sample, which is about 50 times smaller

than the photo-current we measured from the SI-GaAs sample (about 1 mA). This small photo-current is responsible for the small amplitude of the detected signal. However, the pulse width of this sample shown in Figure 4.12(a) is about 5 ps, indicating a vast reduction of the sample carrier lifetime compared to the SI-GaAs sample. Figure 4.12(b) compares the results from the sample with and without the GaAs cap layer. Removing the GaAs superstrate causes large radiation loss into the substrate, resulting in the anticipated extinction of the pulse. These results show that the slot-line in a homogeneous medium can support THz pulses, verifying the theory presented in Chapter 3.

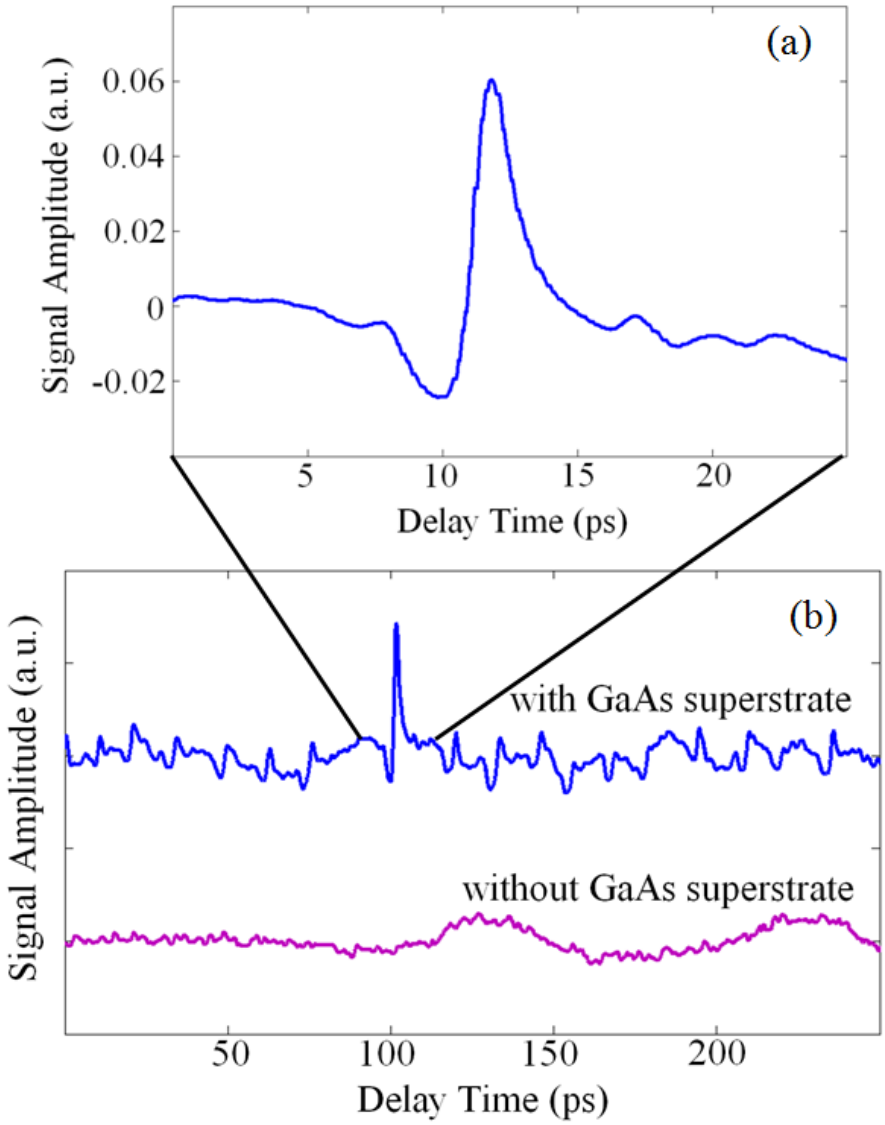

Figure 4.12 (a) Electric field amplitude vs. delay time detected at the receiver for a slot-line with 20 μm gap in LTG-GaAs, (b) comparison of the results with and without superstrate.

Chapter 5

Adiabatic Coupling Tapers

A low-loss two-wire waveguide can capture only a small amount of the power emitted from a highly divergent terahertz dipole source, regardless of its good coupling capability. The terahertz beam cross section after the silicon lens is approximately 25 mm^2 for a typical dipole on a LTG-GaAs substrate. This is a large area compared to the dimensions of the waveguide. The terahertz beam should be focused to the dimensions comparable to the size of the waveguide for good coupling efficiency. Generally, this would require precise alignment of terahertz lenses, with associated loss. Another way to get higher coupling efficiency is to circumvent the antenna part in the system. We need an intermediate device or structure that matches the generated terahertz field to the mode supported by the waveguide. This matching network would deliver power efficiently from the source to the load (the waveguide). Inspired by the structure of slot-lines, we are developing a tapered structure, as shown in Figure 5.1, to couple THz waves from the source to the waveguide.

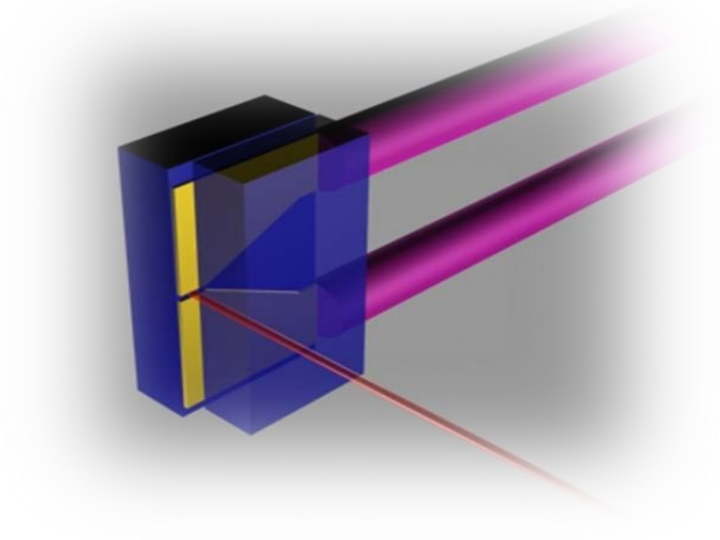

Figure 5.1 Taper structure to couple efficiently THz waves from the source to the two-wire waveguide.

The structure consists of two gold plates separated by a thin slot deposited on an ultra-fast semiconductor substrate such as LTG-GaAs. The slot width starts from 10 μm and increases along the length of the structure in a tapered shape to 400 μm (equal to the edge-to-edge distance of the two wires shown in pink in Figure 5.1). Another GaAs wafer is placed on top of the gold plates as a superstrate. Given the analysis presented in Chapter 3, this cap layer prevents radiation loss into the substrate. A 20V bias voltage applied across the plates can create a ps pulsed current when a fs optical pulse shown in red in Figure 5.1 excites free carriers in the gap. The resulting pulsed current excites the TEM mode of the slot-line that is efficiently coupled to the two-wire waveguide mode by the tapered structure. Note that the optical excitation should be near the cap layer, otherwise radiation loss cannot be effectively avoided by the superstrate.

5.1 Analytic framework

To study the tapered structure we break the taper into many tiny steps, as illustrated in Figure 5.2. Each step can be considered as a slot-line with a different gap width compared to the others. Since the tapered structure starts from a small gap, the TEM mode is the only excited mode, provided the gap width is much smaller than the wavelength. As the gap width increases smoothly along the taper, the TEM mode is expanded corresponding to the gap width. According to the analysis described in Chapter 3 and Figure 3.7(a), a larger gap results in lower loss. However, a larger gap allows the waveguide to support higher-order modes and prevents single-mode operation. The advantage of using a tapered structure is that we excite only a single TEM mode at the beginning and decrease the loss by increasing smoothly the gap while maintaining single-mode operation. Also, with this method of coupling we exploit both the excellent coupling coefficient of the slot-line and the low loss property of the two-wire waveguide.

To obtain the reflection and transmission of the tapered structure, we use transmission matrices [42] as interface between two consecutive slot-lines with step size d and transmission matrices for the wave propagation along each slot-line with length dz.

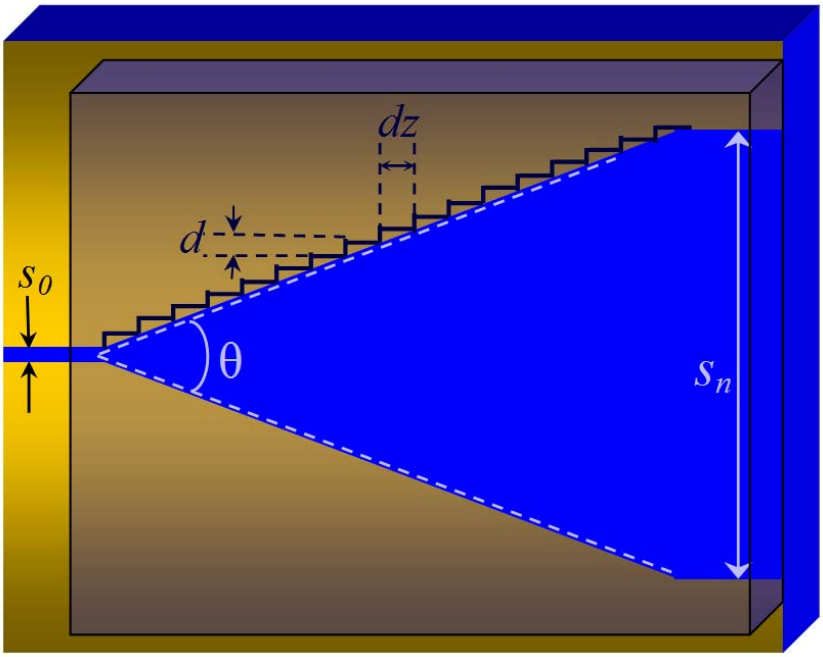

Figure 5.2 Breaking the tapered structure into *n* slot-lines with *s* + *nd* gap width and same *dz* length.

5.2 Transmission matrix at the interface of two slot-lines

Obtaining the transmission matrix of the tapered structure entails knowing the transmission matrix at the interface between two consecutive slot-lines. We use the same single-mode-matching technique described in Chapter 2, Section 2.3. Matching transverse components of the electric and magnetic fields at the intersection of the two slot-lines gives the transmission and reflection. We assume two slot-lines in a homogeneous medium with gap widths s_1 and s_2. An incident TEM mode with 1 W power is incident on the interface of the two slot-lines from the left side, resulting in transmitted and reflected fields with coefficients *t* and *r*, respectively as shown in Figure 5.3. Eqs. 2.24 to 2.35 carry over for this case:

$$t = \frac{2\kappa}{1+\kappa^2}, \tag{5.1}$$

$$r = \frac{1-\kappa^2}{1+\kappa^2}, \tag{5.2}$$

where,

$$\kappa = \frac{1}{2}\iint\left(\vec{e}_{2TEM}\times\vec{h}_{1TEM}^{\,*}\right)\cdot\vec{dS}\,, \tag{5.3}$$

where the integration is over the interface surface shown in Figure 5.4, and e_{2TEM} and h_{1TEM} are the electric and magnetic field of TEM modes supported by slot-lines with gaps s_2 and s_1.

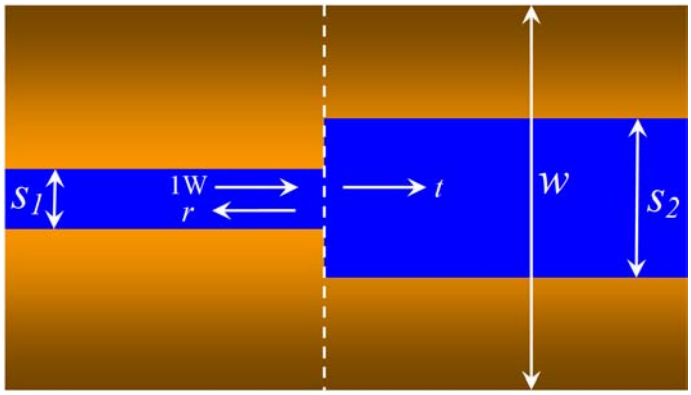

Figure 5.3 1 W incident TEM mode hits the interface of the two slot-lines from left, leading to transmitted and reflected fields with coefficients *t* and *r*.

According to Eq. 3.2, the electric fields of the TEM modes supported by the slot-lines can be expressed as

$$\vec{e}_{1,2TEM} = A_{1,2}\left[\frac{\partial}{\partial x}\left[\mathrm{Re}\left\{\sin^{-1}\left(\frac{x+iy}{s_{1,2}/2}\right)\right\}\right]\hat{x}+\frac{\partial}{\partial y}\left[\mathrm{Re}\left\{\sin^{-1}\left(\frac{x+iy}{s_{1,2}/2}\right)\right\}\right]\hat{y}\right], \tag{5.4}$$

where $A_{1,2}$ are the normalization coefficients that can be determined by

$$A_{1,2} = \sqrt{\frac{\eta}{\pi\cosh^{-1}\left(w/s_{1,2}\right)}}\,, \tag{5.5}$$

where w is the width of the lines. The coupling coefficient κ is

$$\kappa = \frac{1}{2\eta}\iint_S\left(e_{x1}e_{x2}+e_{y1}e_{y2}\right)dxdy\,, \tag{5.6}$$

or,

$$\kappa = \frac{A_1A_2}{2\eta}\iint_S\left(\frac{\partial f_1}{\partial x}\cdot\frac{\partial f_2}{\partial x}+\frac{\partial f_1}{\partial y}\cdot\frac{\partial f_2}{\partial y}\right)dxdy\,, \tag{5.7}$$

where

$$\begin{cases} f_1 \equiv \mathrm{Re}\left\{\sin^{-1}\left(\dfrac{x+iy}{s_1/2}\right)\right\} \\ f_2 \equiv \mathrm{Re}\left\{\sin^{-1}\left(\dfrac{x+iy}{s_2/2}\right)\right\} \end{cases}.$$

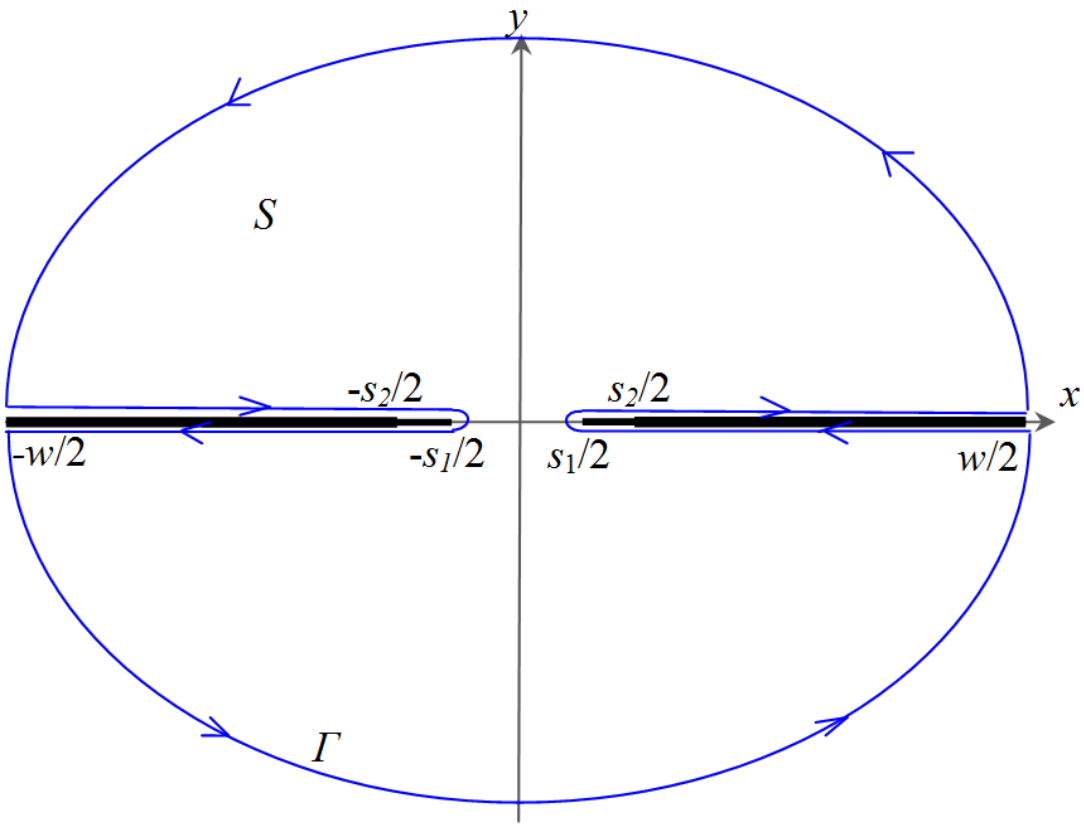

Figure 5.4 The interface plane of two slot-lines S, and Γ is the perimeter of the surface.

Using the following identities and Green's theorem, we can change the surface integral in Eq. 5.7 to a simpler line integral over the perimeter of the surface, Γ:

$$\frac{\partial f_1}{\partial x}\cdot\frac{\partial f_2}{\partial x} = \frac{\partial}{\partial x}\left(f_1\frac{\partial f_2}{\partial x}\right) - f_1\frac{\partial^2 f_2}{\partial x^2}, \tag{5.8}$$

$$\frac{\partial f_1}{\partial y}\cdot\frac{\partial f_2}{\partial y} = \frac{\partial}{\partial y}\left(f_1\frac{\partial f_2}{\partial y}\right) - f_1\frac{\partial^2 f_2}{\partial y^2}. \tag{5.9}$$

Therefore, the coupling coefficient κ can be written as

$$\kappa = \frac{A_1 A_2}{2\eta}\left[\iint_S \left[\frac{\partial}{\partial x}\left(f_1 \frac{\partial f_2}{\partial x}\right) + \frac{\partial}{\partial y}\left(f_1 \frac{\partial f_2}{\partial y}\right)\right] dS - \iint_S f_1 \nabla^2 f_2 \, dS\right]. \tag{5.10}$$

f_2 is an analytic function whose Laplacian is zero that yields

$$\kappa = \frac{A_1 A_2}{2\eta}\left[\iint_S \left[\frac{\partial}{\partial x}\left(f_1 \frac{\partial f_2}{\partial x}\right) - \frac{\partial}{\partial y}\left(-f_1 \frac{\partial f_2}{\partial y}\right)\right] dS\right]. \tag{5.11}$$

Using Green's theorem, described in Chapter 2 Section 2.3, κ is simplified to

$$\kappa = \frac{A_1 A_2}{2\eta}\left[\oint_\Gamma \left(-f_1 \frac{\partial f_2}{\partial y} dx + f_1 \frac{\partial f_2}{\partial x} dy\right)\right], \tag{5.12}$$

where Γ is the contour shown in Figure 5.4. Taking line integral over path Γ yields

$$\kappa = \frac{Ln\left(\frac{w}{s_2} + \sqrt{\left(\frac{w}{s_2}\right)^2 - 1}\right)}{\sqrt{Cosh^{-1}\left(\frac{w}{s_1}\right) Cosh^{-1}\left(\frac{w}{s_2}\right)}}. \tag{5.13}$$

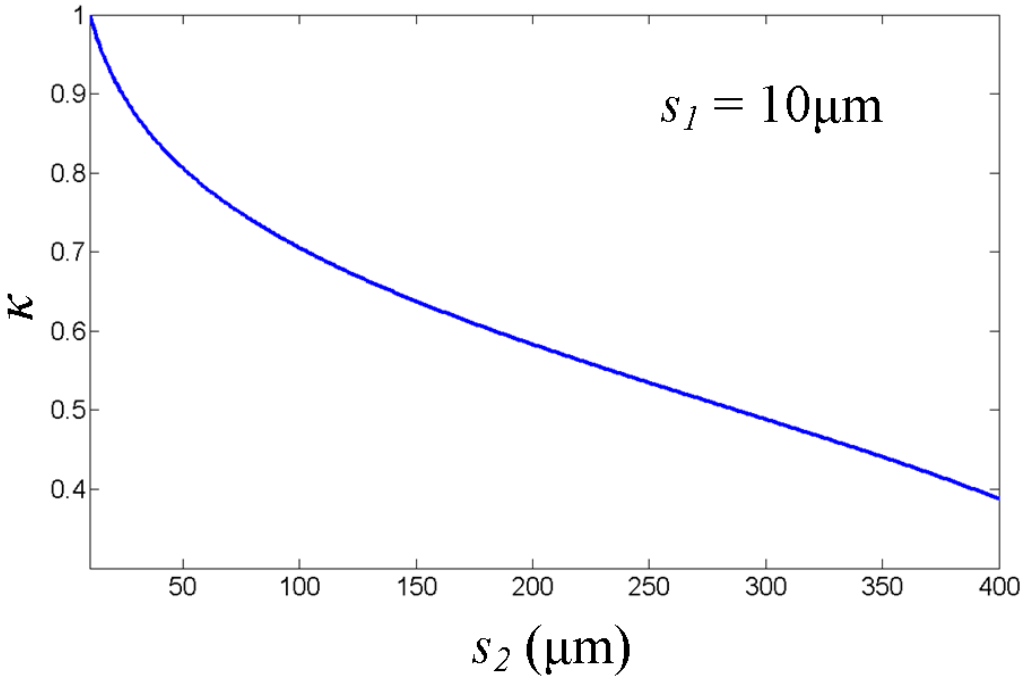

Figure 5.5 κ vs. s_2 when s_1 = 10 μm and w = 500 μm.

Figure 5.5 shows the coupling κ vs. s_2 when s_1 = 10 μm and w = 500 μm. When the gap of the second slot-line is equal to the gap of the first one ($s_1 = s_2$ = 10 μm), the coupling is perfect. However, as the gap of the second slot-line becomes larger compared to the first one, the more severe resulting discontinuity decreases the coupling.

The transmission matrix at the interface of the two slot-lines relates forward and backward fields of the left side to those of the right side as shown in Figure 5.6:

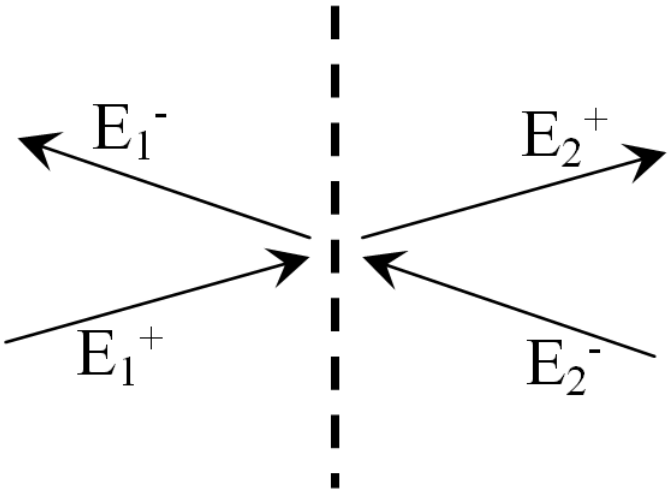

Figure 5.6 Transmission matrix at the interface of the slot-lines.

$$\begin{bmatrix} E_2^{\,+} \\ E_2^{\,-} \end{bmatrix} = T_{\text{interface}} \begin{bmatrix} E_1^{\,+} \\ E_1^{\,-} \end{bmatrix} = \begin{bmatrix} t_{12} - \dfrac{r_{12} r_{21}}{t_{21}} & \dfrac{r_{21}}{t_{21}} \\ -\dfrac{r_{12}}{t_{21}} & \dfrac{1}{t_{21}} \end{bmatrix} \begin{bmatrix} E_1^{\,+} \\ E_1^{\,-} \end{bmatrix}, \tag{5.14}$$

where r_{12}, r_{21}, t_{12}, and t_{21} are reflections and transmissions from medium 1 to 2 and from 2 to 1:

$$r_{12} = \frac{1-\kappa^2}{1+\kappa^2} = -r_{21}, \tag{5.15}$$

$$t_{12} = t_{21} = \frac{2\kappa}{1+k^2}. \tag{5.16}$$

Substituting Eqs. 5.15 and 5.16 into Eq. 5.14 yields

$$T_{\text{interface}} = \begin{bmatrix} \dfrac{\kappa^2+1}{2\kappa} & \dfrac{\kappa^2-1}{2\kappa} \\ \dfrac{\kappa^2-1}{2\kappa} & \dfrac{\kappa^2+1}{2\kappa} \end{bmatrix}. \tag{5.17}$$

5.3 Propagation matrix of a slot-line

The propagation matrix relates forward and backward fields before and after propagation through *dz* length of the slot-line, as shown in Figure 5.7. Obviously, the forward and backward fields satisfy the following relationships:

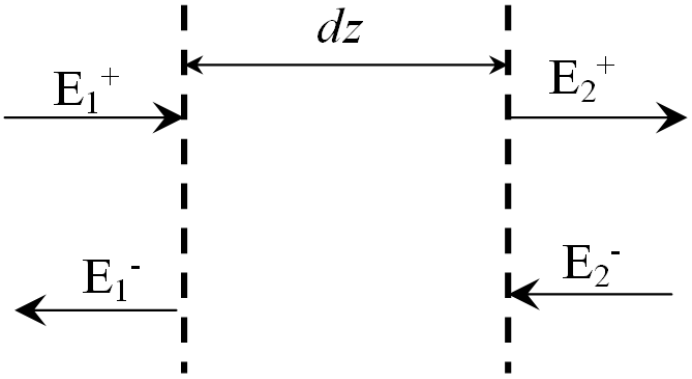

Figure 5.7 Propagation matrix of the slot-line.

$$E_2^{+} = e^{-i\beta dz} \cdot e^{-\alpha dz} E_1^{+}, \tag{5.18}$$

$$E_2^{-} = e^{i\beta dz} \cdot e^{\alpha dz} E_1^{-}, \tag{5.19}$$

that yields

$$T_{\text{propagation}} = \begin{bmatrix} e^{-(\alpha+i\beta)dz} & 0 \\ 0 & e^{(\alpha+i\beta)dz} \end{bmatrix}, \tag{5.20}$$

where α is the waveguide loss that can be obtained by Eq. 3.14 and $\beta = \omega/c$.

5.4 Transmission matrix of the tapered structure

The total transmission matrix of the tapered structure can be obtained by multiplication of interface matrices and propagation matrices:

$$T_{\text{Taper}} = T_{01} T_{\text{propagation}} T_{12} T_{\text{propagation}} \cdots T_{(n-1)n} T_{\text{propagation}}. \tag{5.21}$$

Figure 5.8 shows the transmission and reflection coefficient of a tapered structure in GaAs vs. the length of the taper, L, with s_0 = 10 μm and s_n = 400 μm, obtained from the transmission matrix. In Eq. 5.21, both conductor and dielectric loss are considered in the calculation of the taper transmission matrix. Eq 3.14 in Chapter 3 gives the conductor loss for different slot widths and dielectric loss of GaAs as 0.5 cm^{-1} in the THz range

[51]. As the length of the taper increases, two slot-lines with different gaps (s_0 and s_n) are connected in a smoother way by the tapered structure, resulting in higher transmission and lower reflection. However, since the slot-line has absorption, the transmission decreases as the length increases. Figure 5.8 shows that a length in the range of 250 μm to 500 μm would be a proper choice for the taper with s_0 = 10 μm and s_n = 400 μm. Figure 5.9 compares the reflection versus the length of the taper connecting 10 μm gap to 400 μm gap obtained from the theory and from numerical simulations using Ansoft HFSS. Results are in good agreement for small values of taper length. However, for larger lengths simulation results show higher reflection. first, we attributed this discrepancy to the small reflection of the radiation boundary at the end of the taper. We changed that boundary to a wave port to absorb all the power at the end of the structure, but it did not change the reflection significantly and left this difference a mystery for us.

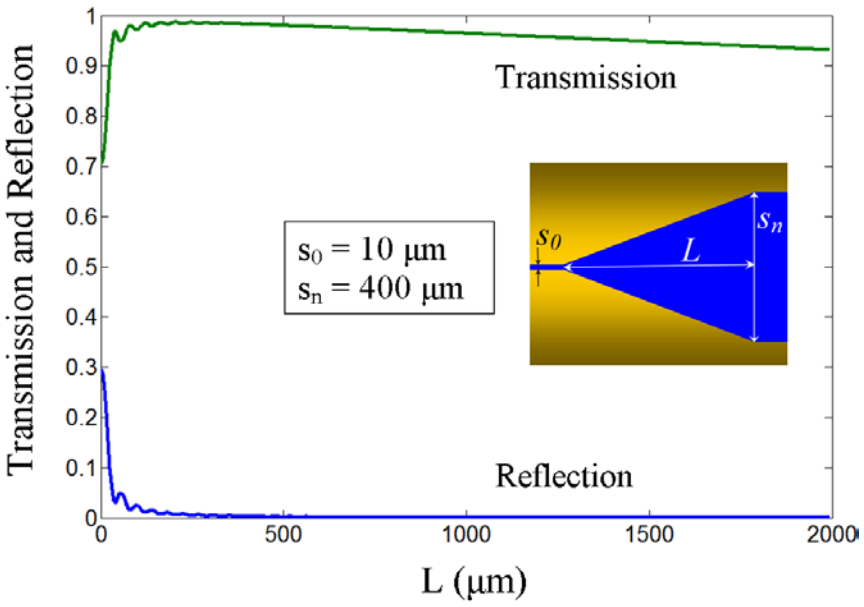

Figure 5.8 Transmission and reflection coefficients of a tapered structure vs. L, the length of the taper, with s_1 = 10 μm and s_2 = 400 μm.

The taper transmission matrix in Eq. 5.21 depends on the dielectric loss of the substrate through propagation matrices. For a slot-line in a lossy medium, the taper length is severely limited by dielectric loss. Figure 5.10 shows the transmission coefficient vs. the length of the taper for the same structure but with different substrate absorption coefficients. For a taper in a lossy medium with 10 cm^{-1} dielectric absorption, the length

of the taper is limited to 35 μm for maximum transmission coefficient (max. transmission = 0.9).

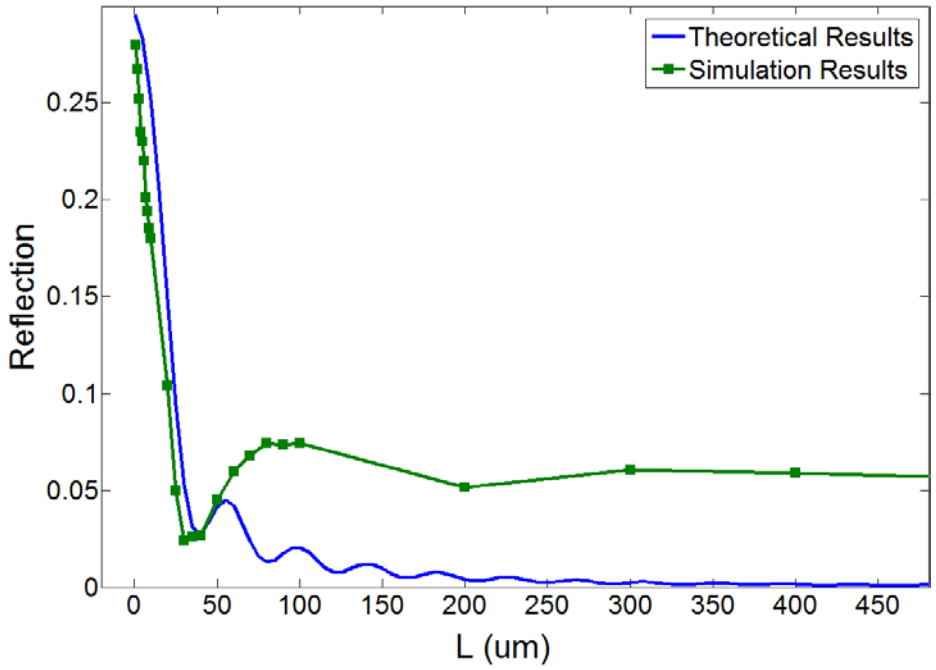

Figure 5.9 Reflection coefficient vs. *L*, the length of the taper, with s_1 = 10 μm and s_2 = 400 μm obtained from the theory (blue line), and from numerical simulations (green) using Ansoft HFSS.

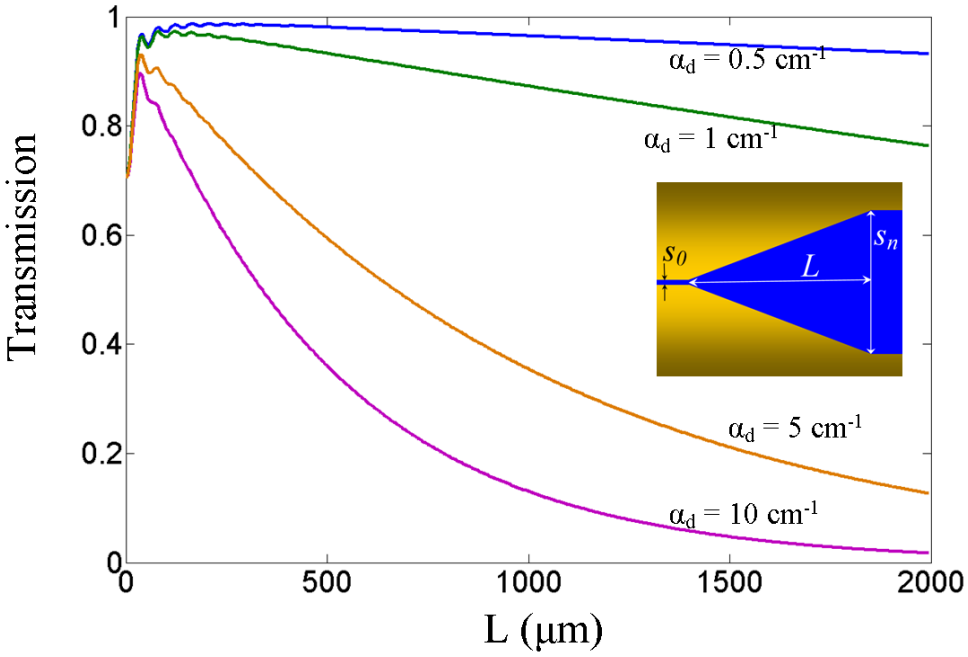

Figure 5.10 Transmission coefficient vs. *L*, the length of the taper, with s_1 = 10 μm and s_2 = 400 μm for dielectric absorption coefficients 0.5 cm^{-1}, 1 cm^{-1}, 5 cm^{-1}, 10 cm^{-1}.

Chapter 6

THz Cable

Waveguides are designed to carry electromagnetic waves from one point to the other without significant loss and comprise an important part of electromagnetic systems. Coaxial cables and optical fibers play a revolutionary role in advancing microwave and optical systems. Unfortunately, at the present time there is no low-loss cable operating in the THz frequency range. However, the two-wire waveguide presented in Chapter 2 can be a legitimate candidate for making a THz cable. It offers both low-loss and good coupling since the distribution of the TEM mode supported by this waveguide is well-matched to the output of most photoconductive antennas or the taper explained in Chapter 5. We have evaluated the performance of the two-wire waveguide theoretically, with numerical simulation, and experimentally at THz frequencies [23,60,61]. Results show that absorption as low as 0.01 cm^{-1} at 1THz is achievable for the two-wire waveguide with appropriate dimensions, suggesting waveguide loss can no longer be a concern and a THz cable can be realized.

In this chapter, we propose practical structures for a THz cable based in a two-wire waveguide. We evaluate different structures and presents theoretical and simulation results.

6.1 Two-wire waveguide TEM mode and loss:

Figure 2.4 in Chapter 2 shows the electric field distribution of the TEM mode supported by the two-wire waveguide for 400 μm radii (R) of the wires and different center-to-center distance (D). When the wires are close, the field is largely concentrated in the area between the wires. However, as the wire spacing increases, the field becomes more evenly distributed around the wires. This leads to lower conductor loss for higher center-to-center separations of the wires [23]. Figure 2.5 shows the conductor loss of the two-wire waveguide made out of gold versus center-to-center distance of the wires at 1THz.

Conductor loss less than 0.01 cm^{-1} can be achieved by a two-wire waveguide with more than 200 μm radii of the wires and more than 1 mm center-to-center distance.

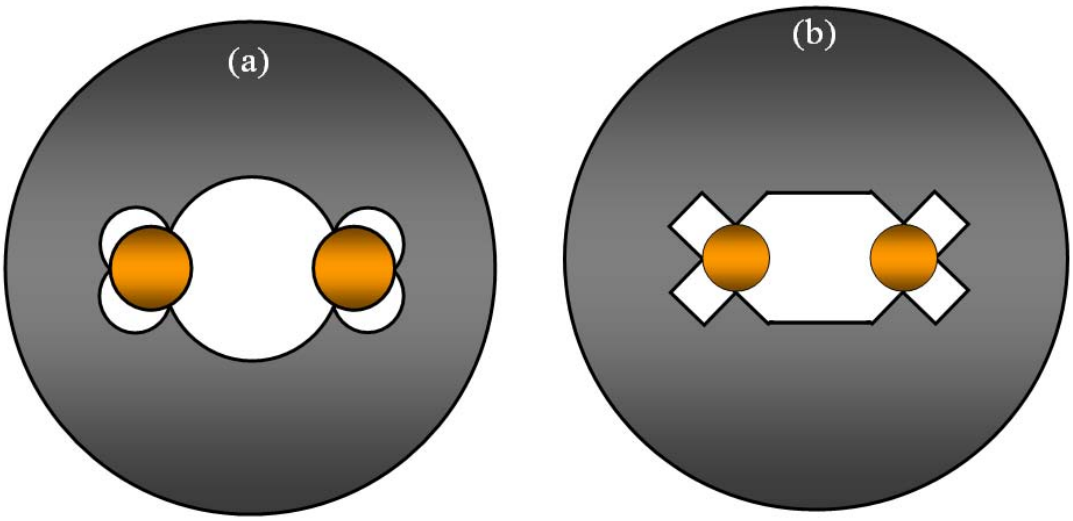

Figure 6.1 Cross section of two suitable structures for THz two-wire waveguide cable, grey material is PMI and white area is air.

6.2 THz cable structures

Free space is the best medium to carry electromagnetic waves for long-range broadband applications, since it has neither dielectric loss nor material dispersion. However, a material is required to hold the wires in position. We propose polymethacrylimide rigid foam (PMI) as the material for holding the two wires, since it has remarkably low permittivity (1.03) and low dielectric loss tangent (less than 0.5%) in the 0.1-2 THz range [62]. Due to its low permittivity, PMI would not change the TEM mode distribution of the two-wire waveguide. PMI is also capable of being formed in different shapes by define machines.

Equation 2.23 gives the conductor loss for a TEM mode of the two-wire waveguide. The conductor loss is inversely proportional to the intrinsic impedance of the propagating medium. Therefore, the conductor loss increases by the factor n, the refractive index of the medium, since electromagnetic waves see longer effective length when propagating through a medium with $n > 1$. For the two-wire waveguide surrounded completely by PMI, the conductor loss then increases by 1.4%. The total loss for the TEM mode also includes an additional dielectric loss equal to

$$\alpha_d = \frac{\omega \cdot (\text{loss tangent})}{2v}, \tag{6.1}$$

where v is the phase velocity. The loss tangent of PMI was measured to be less than 0.01 in the 0.1-2 THz range [62], resulting in 1 cm^{-1} dielectric loss for the two-wire waveguide in PMI. Therefore, dielectric loss is the dominant absorption mechanism; if the dimensions of the waveguide are chosen appropriately to have low conductor loss according to the Figure 2.5. This absorption is not tolerable for a 10 cm-long THz cable. Therefore, a suitable structure for a THz two-wire cable would have most of the field propagate through air and have the least area of PMI for holding the wires. We propose two mechanically pragmatic structures shown in Figure 6.1.

To estimate loss of the proposed structures we use the effective index method. In this method the concentration of the field is determined in dielectric and air. The concentration factors defined as [63]:

$$\Gamma_{PMI} = \frac{\int_{PMI} |E|^2 \, dxdy}{\int_{xy} |E|^2 \, dxdy}, \tag{6.2}$$

$$\Gamma_{air} = \frac{\int_{air} |E|^2 \, dxdy}{\int_{xy} |E|^2 \, dxdy}, \tag{6.3}$$

are an appropriate measure of the degree of field concentration in the dielectric and air. The effective refractive index is then [63]

$$n_{eff} = \sqrt{\Gamma_{PMI}\varepsilon_{PMI} + \Gamma_{air}\varepsilon_{air}}\,. \tag{6.4}$$

Figure 6.2(a) shows air and PMI concentration factors versus D, the center-to-center distance of the wires, for the structure shown in Figure 6.1(b) with 400 μm radii of the wires. As D increases the field becomes more distributed around the wires (according to the Fig. 2.4), enhancing the concentration factor of PMI. This leads to higher dielectric loss as electromagnetic energy propagates more through the lossy dielectric.

According to Figure 2.4, smaller center-to-center distance results in higher field concentration in air and lower dielectric loss. However, small D also leads to higher

conductor loss according to Figure 2.5. Conductor loss, dielectric loss, and total loss versus *D* are illustrated in Figure 6.2(b). It shows that minimum total loss is about 0.1cm^{-1} and occurs at $D = 900$ μm.

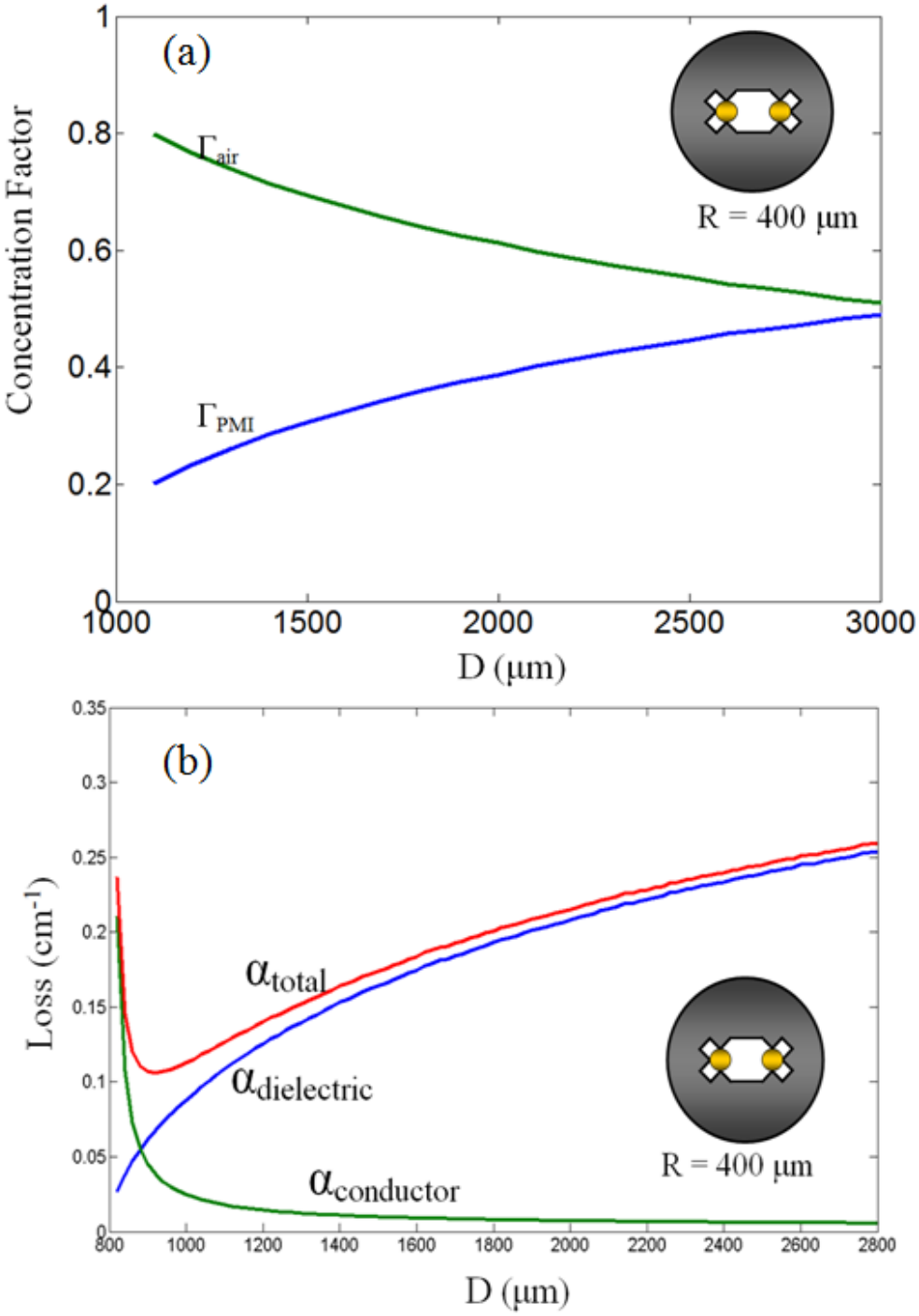

Figure 6.2 (a) Air and PMI concentration factors vs. *D*, (b) Conductor loss, dielectric loss, and total loss vs. *D* for the structure shown in Fig. 6.1(b) with 400 μm radii of the wires.

These results show good agreement with 3D full-wave numerical simulations using the Finite Element Method (FEM). Figure 6.3(a) shows the electric field distribution of a THz cable structure illustrated in Figure 6.1(b). The TEM mode of the two-wire waveguide in air is excited in an air-filled transition region and propagates along the waveguide toward the PMI cable structure. The PMI part does not change significantly the distribution of the TEM mode supported by the two-wire waveguide, due to its low permittivity, validating the concentration factor calculations. We compared loss for three cases: two-wire waveguide in air, in PMI, and in the structure shown in Figure 6.1(b), using numerical simulations for a waveguide with 40 μm radii of the wires and 200 μm center-to-center distance. The results show that a loss of the PMI cable structure is about 40% of waveguide completely in PMI, consistent with the calculation shown in Figure 6.2. Figure 6.3(b) shows the simulation for the same structure with the foam replaced by a material with 12.9 permittivity (like GaAs). The high permittivity of the material changes the distribution of the field, draining waves into the material. Therefore, the low permittivity of the foam is critical.

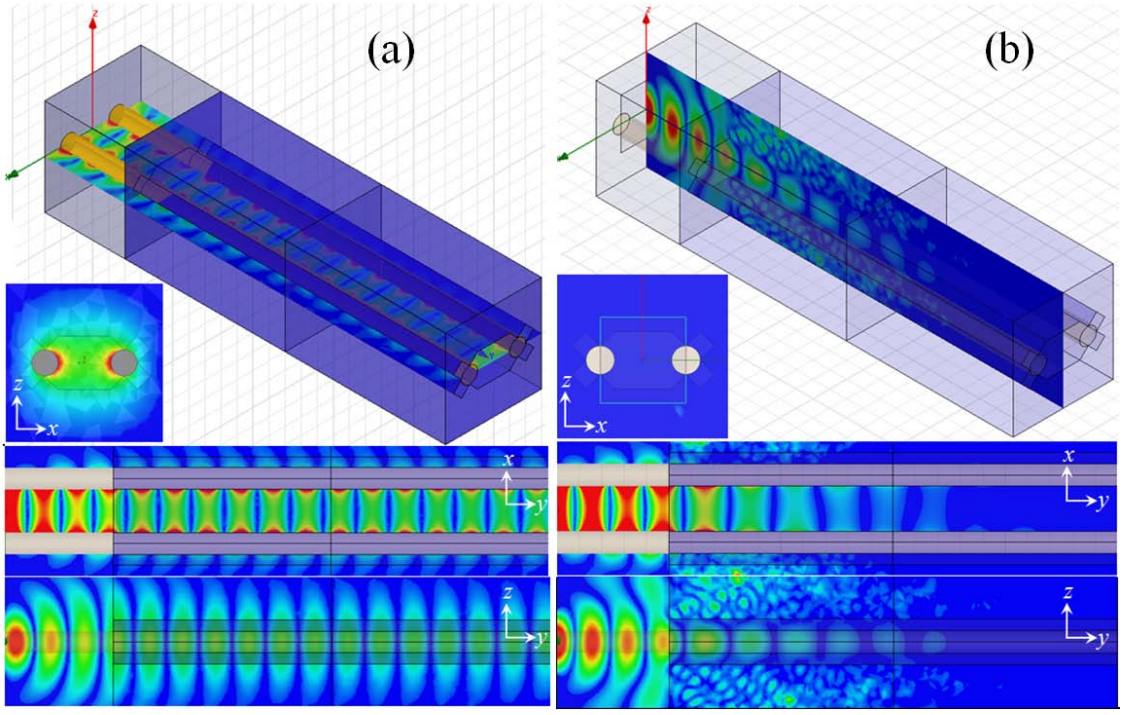

Figure 6.3 3D full-wave numerical FEM simulations using Ansoft HFSS on THz two-wire cable structure shown in Fig. 6.1(b) made out of (a) PMI and (b) a dielectric with ε_r = 12.9.

Figure 6.4 shows the concentration factors and loss for the cable structure shown in Figure 6.1(a). The minimum total loss increases by 50% since PMI covers more area than the structure in Figure 6.1(b).

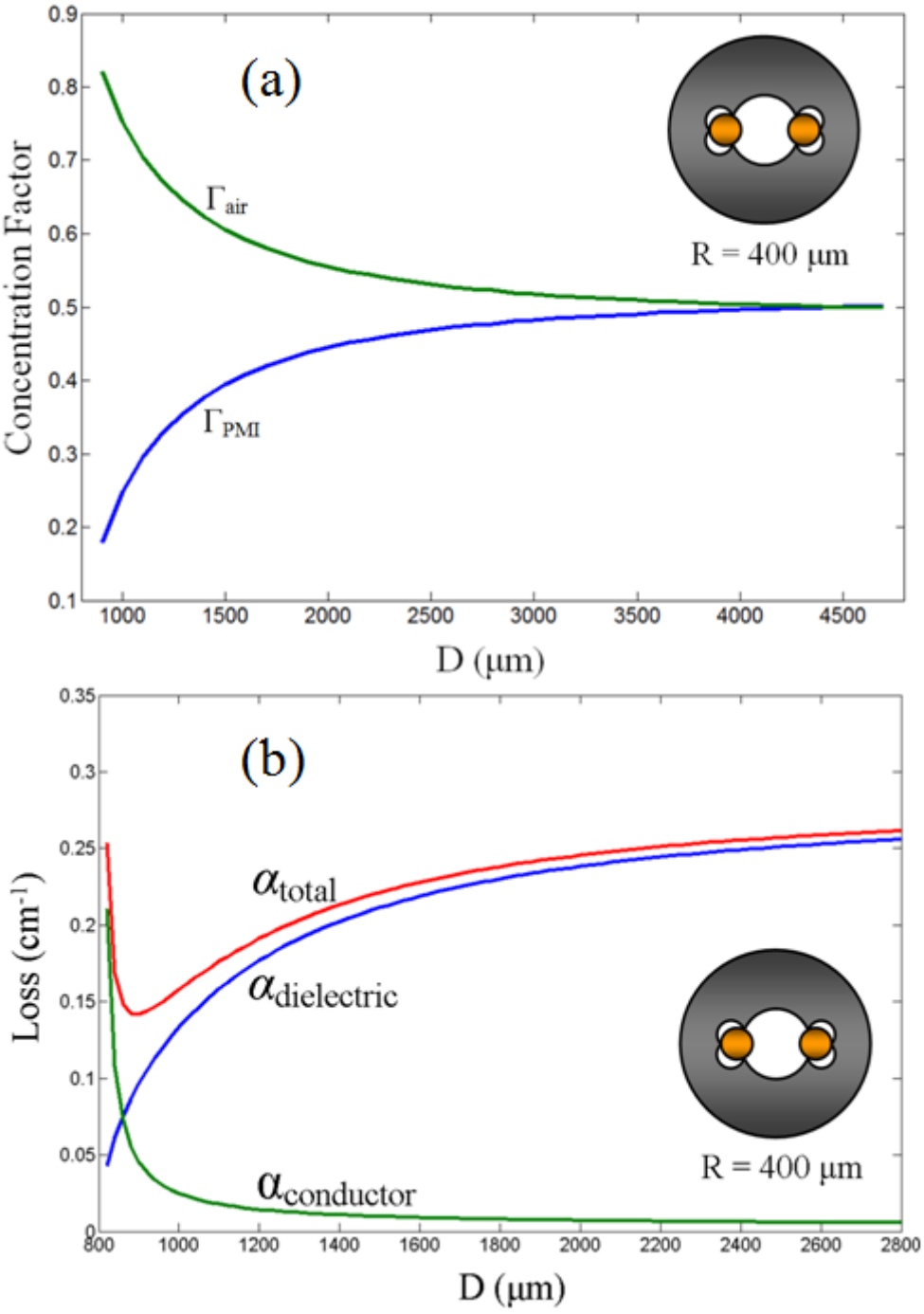

Figure 6.4 (a). Air and PMI concentration factors vs. *D*, (b) conductor loss, dielectric loss, and total loss vs. *D* for the structure shown in Fig. 6.1(a) with 400 μm radii of the wires.

The mechanical support does not need to be used continuously along the cable as is common practice in the microwave range [64]. A couple of PMI blocks located periodically along the cable can hold the wires as shown in Figure 6.5(a) [64]. That decreases dielectric loss associated with PMI. Figure 6.5(b) shows how periodic blocks with 10% and 20% longitudinal duty cycle of PMI can push the minimum of loss to the higher center-to-center distance where conductor loss is significantly lower. Given these results, we can design a THz cable with loss as low as 0.02 cm^{-1}.

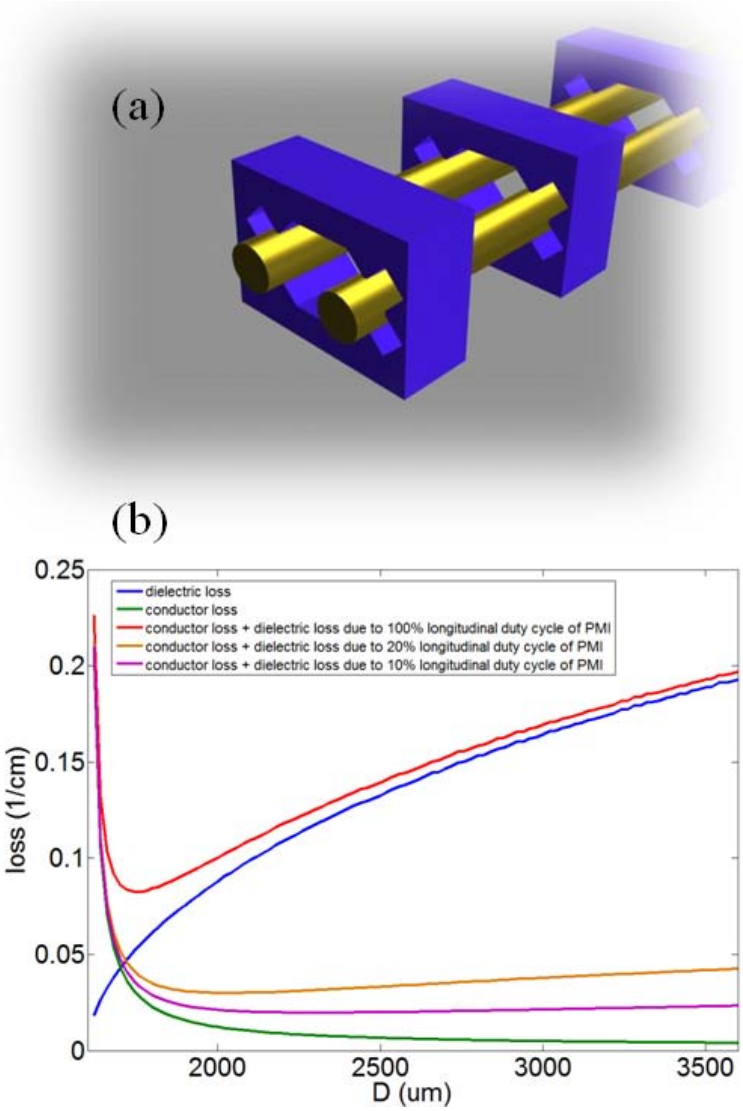

Figure 6.5. (a) PMI blocks located periodically along the THz cable to hold the wires with lower dielectric loss introduced by PMI, (b) dielectric loss (blue), conductor loss (green), conductor loss plus dielectric loss due to 100% (red), 20% (orange), and 10% (purple) longitudinal duty cycle of PMI.

Chapter 7

Conclusions

In this dissertation we present our research on novel waveguide structures operating at terahertz frequencies. The two-wire waveguide is proposed as a low-loss well-behaved THz waveguide that has good coupling efficiency and is free from group velocity dispersion. We also propose two novel planar slot-line structures as low-loss transmission lines for THz waves. Theoretical analysis, numerical simulations, and experimental results are presented to evaluate and confirm the performance of the proposed waveguides.

Using these waveguides can improve significantly existing THz time-domain spectrometers (THz TDS) with THz optics components. In particular, using waveguides can simplify alignment significantly. A compact integrated THz TDS can be achieved using proposed planar slot-line structures. THz electromagnetic energy can also be confined in sub-wavelength dimensions using the two-wire and slot-line waveguides.

The spectroscopy of gas-phase samples can be obtained with the two-wire waveguide in a glass tube presented in Chapter 4. Small biological samples also can be inserted in the area between the two wires for high-resolution THz spectroscopy.

We also present a tapered structure to couple THz waves more efficiently from a photoconductive THz source to the two-wire waveguide. Both the excellent coupling coefficient of the slot-line and the low loss property of the two-wire waveguide can be exploited using the tapered structure in a highly efficient THz system without any radiation loss. Also, the remarkably low absorption of the two-wire waveguide suggests that this waveguide can be used to realize the first THz low loss cable, a critical first step towards making THz passive components like divider/combiners and couplers.

Chapter 8

Main Contributions:

Our main contributions, presented in this dissertation are:

- exploring fully the two-wire waveguide as a low-loss, non-dispersive waveguide for THz frequencies,
- introducing and evaluating two novel slot-line structures for THz waves,
- presenting experimental verification for the two-wire waveguide and the slot-line,
- proposing a tapered structure to couple more efficiently THz waves from a photoconductive source to a two-wire waveguide, and finally,
- proposing the first low loss THz cable.

The research work presented in this dissertation resulted in the following publications and patent:

1. **H. Pahlevaninezhad**, B. Heshamt, and T. E. Darcie, “Efficient terahertz slot-line waveguides,” Optics Express 19, 26, B47-B55, 2011.
2. T. E. Darcie, **H. Pahlevaninezhad**, and B. Heshmat, “Efficient terahertz waveguides,” 37th ECOC, OSA, 2011 (Invited paper).
3. **H. Pahlevaninezhad**, T. E. Darcie, and B. Heshmat, “Advances in terahertz waveguides and transmission lines,” SPIE Proceeding 8007, 80070S, 2011 (Invited paper).
4. **H. Pahlevaninezhad**, B. Heshmat, and T. E. Darcie, “Advances in terahertz waveguides and sources,” IEEE Photonic Journal, Breakthrough in Photonics 2010, 2011 (Invited paper).
5. B. Heshmat, **H. Pahlevaninezhad**, J. Zhang, and T. E. Darcie, “Dynamics of noise in THz photomixers as a receiver sensor,” Optical Sensors, OSA, 2011.
6. **H. Pahlevaninezhad**, T. E. Darcie, and B. Heshmat, “Two-wire waveguide for terahertz,” Optics Express 18, 7, 7415-7420, 2010.

7. **H. Pahlevaninezhad**, and T. E. Darcie, “Coupling of terahertz waves to a two-wire waveguide,” Optics Express 18, 22, 22614-22624, 2010.
8. **H. Pahlevaninezhad**, B. Heshmat, and T. E. Darcie, “Modeling terahertz heterodyne detection based on photomixing,” IEEE Radar Conference, 113-116, 2010.
9. T. E. Darcie, **H. Pahlevaninezhad**, B. Heshmat, and J. Zhang, “Advances in terahertz technology,” 23rd Annual Meeting of IEEE Photonics Society, 435-436, 2010 (Invited paper).

- T. E. Darcie, **H. Pahlevaninezhad**, “Photomixer-Waveguide Coupling Tapers,” US Provisional Patent, Filing No. 61406535, Oct. 2010.

Bibliography

1. B. J. Thompson, Terahertz Spectroscopy: Principles and applications, CRC Press, 2008.

2. D. Dragoman, and M. Dragoman, “Terahertz fields and applications, ” Progress in Quantum Electronics 28, 1-66, 2004.

3. R. M. Woodward, V. P. Wallace, R. J. Pye, B. E. Cole, D. D. Arnone, E. H. Linfield, and M. Pepper, “Terahertz pulse imaging of *ex vivo* Basal Cell Carcinoma,” Journal of Investigative Dermatology, 120, 72-78, 2003.

4. V. P. Wallace, A. J. Fitzgerald, S. Shankar, N. Flanagan, R. Pye, J. Cluff, and D. D. Arnone, “Terahertz pulse imaging of Basal Cell Carcinoma *ex vivo* and *in vivo*,” British Journal of Dermatology 151, 424-432, 2004.

5. H. Harde, J. Zhao, M. Wolff, R. A. Cheville, and D. Grischkowsky, “THz time-domain spectroscopy on ammonia,” Journal of Physical Chemistry A 105, 6038-6047, 2001.

6. Z. Mics, P. Kuzel, P. Jungwirth, and S. E. Bradforth, “Photoionization of atmospheric gases studied bt time-resolved terahertz spectroscopy,” Chemical Physics Letters 465, 20-24, 2008.

7. S. A. Harmon, and R. A. Cheville, “Part-per-million gas detection from long-baseline THz spectroscopy,” Applied Physics Letters 85, 2128-2130, 2004.

8. R. H. Jacobsen, D. M. Mittleman, and M. C. Nuss, “Chemical recognition of gases and gas mixtures with terahertz waves,” Optics Letters 21, 24, 1996.

9. D. M. Mittleman, R. H. Jacobsen, R. Neelamani, R. G. Baraniuk, and M. C. Nuss, “Gas sensing using terahertz time-domain spectroscopy,” Applied Physics B 67, 379-390, 1998.

10. R. H. Jacobsen, and D. M. Mittleman, “Real-time chemical recognition of gas mixtures using optoelectronic terahertz waveforms, in ultrafast electronics and optoelectronics,” Journal of Optical Society of America 13, UF12, 1997.

11. F. Hindle, A. Cuisset, R. Bocquet, and G. Mouret, “Continuous-wave terahertz by photomixing: Applications to gas phase pollutant detection and quantification,” Elsevier, C. R. Physique 9, 262-275, 2008.

12. R. J. Foltynowics, R. E. Allman, and E. Zuckerman, “Terahertz absorption measurement for gas-phase 2,4-dinitrotoluene from 0.05 THz to 2.7 THz,” Elsevier, Chemical Physics Letters 431, 34-38, 2006.

13. R. A. Cheville, and D. Grischkowsky, “Far-field terahertz time-domain spectroscopy of flames,” Optics Letters 20, 15, 1646-1648, 1995.

14. M. Y. Frankel, S. Gupta, J. A. Valdmanis, and G. A. Mourou, “Terahetz attenuation and dispersion characteristics of coplanar transmission lines,” IEEE Transaction on Microwave Theory and Techniques 39, 910-916, 1991.

15. C G. Gallot, S. P. Jamison, R. W. McGowan, and D. Grischkowsky, “Terahertz waveguides,” Journal of Optical Society of America B 17**,** 851-863, 2000.

16. R. Mendis, and D. Grischkowsky, “Plastic ribbon THz waveguides,” Journal of Applied Physics 88, 4449-4451, 2000.

17. S. P. Jamison, R. W. McGowan, and D. Grischkowsky, “Single-mode waveguide propagation and reshaping of sub-ps terahertz pulses in sapphire fibers, ” Applied Physics Letters 76, 1987-1989, 2000.

18. R. Mendis, and D. Grischkowsky, “Undistorted guided-wave propagation of subpicosecond terahertz pulses,” Optics Letters 26, 846-848, 2001.

19. L. J. Chen, H. W. Chen, T. F. Kao, J. Y. Lu, and C. K. Sun, “Low-loss subwavelength plastic fiber for terahertz waveguiding,” Optics Letters 31, 308-310, 2006.

20. K. Wang, and D. Mittleman, “Metal wires for terahertz wave guiding,” Nature 432, 376-379, 2004.

21. J. A. Deibel, K. Wang, M. D. Escarra, and D. M. Mittleman, “Enhanced coupling of terahertz radiation to cylindrical wire waveguides,” Optics Express 14, 279, 2006.

22. M. K. Mbonye, V. Astley, W. L. Chan, J. A. Deibel, and D. M. Mittleman, “A terahertz dual wire waveguide,” in *Lasers and Electro-Optics Conference*, Optical Society of America, 2007, paper CThLL1.

23. H. Pahlevaninezhad, T. E. Darcie, and B. Heshmat, “Two-wire waveguide for terahertz,” Optics Express 18, 7415-7420, 2010.

24. M. K. Mbonye, R. Mendis, and D. M. Mittleman, “A terahertz two-wire waveguide with low bending loss,” Applied Physics Letters 95, 233506, 2009.

25. M. Martl, J. Darmo, D. Dietze, K. Unterrainer, and E. Gornik, “Terahertz waveguide emitter with subwavelength confinement,” Journal of Applied Physics 107, 013110, 2010

26. H. Pahlevaninezhad, B. Heshamt, and T. E. Darcie, “Efficient terahertz slot-line waveguides,” Optics Express 19, 26, B47-B55, 2011.

27. S. Ramo, J. R. Whinnery, and T. V. Duzer, Fields and waves in communication electronics, Second Edition, Jon Wiley, 1984.

28. E. B. Saff, and A. D. Snider, Fundamental of complex analysis: With applications to engineering and science, Third Edition, Prentice Hall, 2003.

29. J. D. Jackson, Classical electrodynamics, Third Edition, Academic, pp. 352-356, 1999.

30. R. E. Collin, Field theory of guided waves, Second Edition, IEEE Press, pp. 256-263, 1991.

31. S. Matsuura, M. Tani, and K. Sakai, “Generation of coherent terahertz radiation by photomixing in dipole photoconductive antenna,” Applied Physics Letters 70, 559, 1997.

32. S. M. Duffy, S. Verghese, A. McIntosh, A. Jackson, A. C. Gossard, and S. Matsuura, “Accurate modeling of dual dipole and slot elements used with photomixers for coherent terahertz output power,” IEEE Transaction on Microwave Theory and Techniques 49, 6, 1032-1038, 2001.

33. S. Matsuura, and H. Ito, “Generation of CW terahertz radiation with photomixing,” Topics Applied Physics 97, 157-204, 2005.

34. W. Lukosz, and R. E. Kunz, “Light emission by magnetic and electric dipoles close to a plane interface. I. Total radiated power,” Journal of Optical Society of America 67, 1607-1614 ,1977.

35. W. Lukosz, and R. E. Kunz, “Light emission by magnetic and electric dipoles close to a plane interface. II. Radiation patterns of perpendicular oriented dipoles,” Journal of Optical Society of America 67**,** 1615-1619, 1977.

36. W. Lukosz, “Light emission by magnetic and electric dipoles close to a plane interface. III. Radiation patterns of dipoles with arbitrary orientation,” Journal of Optical Society of America 69**,** 1495-1502, 1979.

37. J. Y. Courtois, J. M. Courty, and J. C. Mertz, “Internal dynamics of multilevel atoms near a vacuum-dielectric interface,” Physical Review A 53, 1862-1878, 1996.

38. L. Luan, P. R. Sievert, and J. B. Ketterson, “Near-field and far-field electric dipole radiation in the vicinity of a planar dielectric half space,” Journal of Physics 8, 264, 2006.

39. P. U. Jepsen, and S. R. Keiding, “Radiation patterns from lens-coupled terahertz antennas,” Optics Express 20, 807-809, 1995.

40. C. Fattinger, and D. Grischkowsky, “Terahertz beams,” Applied Physics Letters 54, 490, 1989.

41. P. U. Jepsen, R. H. Jacobsen, and S. R. Keiding, “Generation and detection of terahertz pulses from biased semiconductor antennas,” Journal of Optical Society of America B 13, 2424-2436, 1996.

42. A. Yariv, and P Yeh, Optical waves in crystals: Propagation and control of laser radiation, John Wiley & Sons, Chap. 11, 1984.

43. D. M. Pozar, Microwave engineering: Third Edition, John Wiley & Sons, Chap. 4, 2005.

44. D. R. Grischkowsky, M. B. Ketchen, C. C. Chi, I. N. Duling, I. Naomi, J. Halas, J. M. Halbout, and P. G. May, “Capacitance free generation and detection of subpicosecond electrical pulses on coplanar transmission lines,” IEEE Journal of Quantum Electronics 24, 221-225, 1988.

45. D. Grischkowsky, and I. N. Duling, J. C. Chen, and C. C. Chi, “Electromagnetic shock waves from transmission lines,” Physical Review Letters 59, 1663-1666, 1987.

46. D. Grischkowsky, “Optoelectronic characterization of transmission lines and waveguides by terahertz time-domain spectroscopy,” IEEE Journal on Selected Topics in Quantum Electronics 6, 1122-1135, 2000.

47. J. V. Jelley, Cherenkov radiation and its applications, Pergamon, New York, 1958.

48. C. Fattinger, and D. Grischkowsky, “Observation of electromagnetic shock waves from propagating surface-dipole distributions,” Physical Review Letters 62, 2961-2964, 1989.

49. D. K. Kleinman, and D. H. Auston, “Theory of electro-optic shock radiation in nonlinear optical media,” IEEE Journal of Quantum Electronics QE-20, 964-970, 1984.

50. Z. Ruan, G. Veronis, K. L. Vodopyanov, M. M. Fejer, and S. Fan, “Enhancement of optics-to-THz conversion efficiency by metallic slot waveguides,” Optics Express 17, 13502-13515, 2009.

51. D. Grischkowsky, S. Keiding, M. van Exter, and C. Fattinger, “Far-infrared time-domain spectroscopy with terahertz beams of dielectrics and semiconductors,” Journal of Optical Society of America B **7**, 2006-2015, 1990.

52. J. D. Joannopoulos, S. G. Johnson, J. N. Winn, and R. D. Meade, Photonic crystals: Modeling the flow of light, Second Edition, Princeton Univ. Press, Chap. 4, 2008.

53. P. Yeh, A. Yariv, and C. Hong, “Electromagnetic propagation in periodic media. I. General theory,” Journal of Optical Society of America 67, 423-438, 1977.

54. P. Yeh, Optical waves in layered media, Wiley, Chap. 6, 1988.

55. A. Yariv, and P. Yeh, Optical Waves in Crystals: Propagation and Control of Laser Radiation, Wiley, Chap. 6, 1984.

56. D. M. Pozar, Microwave engineering: Third Edition, John Wiley & Sons, pp. 97-98, 2005.

57. M. Y. Frankel, R. H. Voelker, and J. N. Hilfiker, “Coplanar transmission lines on thin substrates for high-speed low-loss propagation,” IEEE Transaction on Microwave Theory and Techniques 42, 396-402, 1994.

58. G. Loata, “Investigation of low-temperature-grown GaAs photoconductive antennae for continuous-wave and pulsed terahertz generation,” PhD Dissertation, Goethe University, 2002.

59. C. B. Rogers, G. H. B. Thompson, and G. R. Antell, “Dielectric constant and loss of semi-insulating GaAs at microwave frequencies,” Applied Physics Letters 11, 353-354, 1967.

60. H. Pahlevaninezhad, and T. E. Darcie, “Coupling of terahertz waves to a two-wire waveguide,” Optics Express 18, 22, 22614-22624, 2010.

61. H. Pahlevaninezhad, B. Heshmat, and T. E. Darcie, “Advances in terahertz waveguides and sources,” IEEE Photonic Journal, Breakthrough in Photonics 2010, 307-310, 2011.

62. C. Roman, O. Ichim, L. Sarger, V. Vignera, and P. Mounaix, “Terahertz dielectric characterisation of polymethacrylimide rigid foam: The perfect sheer plate?,” Electronics Letters 40, 19, 22-23, 2004.

63. A. Yariv, and P. Yeh, Photonics: Optical electronics in modern communications, Sixth Edition, Oxford University Press, Chap. 3, 2007.

64. P. J. Wood, “TEM line technology for satellite antenna feed applications,” Proceeding Satellite Communication Conference SCC-83, 29.16.1-19.6.4, Ottawa, 1983.